Research Square

Preprints are preliminary reports that have not undergone peer review.
They should not be considered conclusive, used to inform clinical practice,
or referenced by the media as validated information.

Machine-Learning-Based Landslide Susceptibility Mapping Using an InSAR- Refined Inventory in the Mandi district, Northwestern Himalaya, India, Himalaya region

Akshay Raj Manocha

akshayrajgeology@gmail.com

University of Silesia in Katowice

Tran Trung Hieu

University of Silesia in Katowice

Łukasz Pawlik

University of Silesia in Katowice

Paweł Kroh

University of the National Education Commission

Article

Keywords: landslide susceptibility, machine learning, InSAR, ground deformation

Posted Date: July 30th, 2026

DOI: https://doi.org/10.21203/rs.3.rs-10347129/v1

License: This work is licensed under a Creative Commons Attribution 4.0 International License.
Read Full License

Additional Declarations: No competing interests reported.

Machine-Learning-Based Landslide Susceptibility Mapping Using an InSAR-Refined Inventory in the Mandi district, Northwestern Himalaya, India, Himalaya region

Akshay Raj Manocha[1,2*], Tran Trung Hieu [1,2,3], Łukasz Pawlik [2], Paweł Kroh [4]

[1] International Environmental Doctoral School, University of Silesia in Katowice, Sosnowiec, Poland.

[2] Institute of Earth Sciences, University of Silesia in Katowice, Sosnowiec, Poland.

[3] Institute of Earth Science, Vietnam Academy of Science and Technology, Hanoi, Vietnam.

[4] Institute of Biology and Earth Sciences, University of the National Education Commission, Kraków, Poland.

*Corresponding author e-mail: akshayrajgeology@gmail.com

Abstract

Landslides triggered by intense monsoon rainfall and active tectonics pose a persistent threat to transportation corridors and settlements in the Mandi district of the Northwestern Himalaya. Most existing susceptibility assessments for this region rely on static geomorphological and historical inventories, overlooking pre-failure slope deformation that may indicate emerging instability. This study presents the first landslide susceptibility assessment for Mandi district that integrates Interferometric Synthetic Aperture Radar (InSAR) derived ground deformation with machine learning to produce a more dynamic and reliable hazard map. Sentinel-1 SAR data from 2023–2024 were processed using Persistent Scatterer Interferometry (StaMPS) and Small Baseline Subset analysis (MintPy) to detect active deformation, which was used to refine the Geological Survey of India's Bhukosh landslide inventory, adding 36 previously unmapped landslides and increasing inventory completeness by 18%. Twelve uncorrelated topographic, hydrological, geological, climatic, and anthropogenic conditioning factors were selected using Pearson correlation and variance inflation factor analysis. Four machine learning algorithms, Extreme Gradient Boosting (XGB), Random Forest, Logistic Regression, and Multilayer Perceptron, were trained and compared using a nested spatial block cross-validation framework across block sizes of 1,000–10,000 m. XGB achieved the best performance at an optimal block size of 3,000 m, and the InSAR-refined inventory improved model AUC by 12–15% relative to a conventional inventory. SHAP, mean decrease accuracy, and accumulated local effects analyses identified slope, distance to roads, distance to faults, and rainfall as the dominant controls on landslide occurrence. The resulting five-class susceptibility map shows that high- and very high-susceptibility zones, covering about 25% of the district, contain the vast majority of mapped landslides, with frequency ratios of 1.55 and 6.5, respectively. These results demonstrate that coupling InSAR-derived deformation with machine learning substantially improves the accuracy and currency of landslide susceptibility mapping, offering a scalable approach for hazard mitigation and land-use planning in tectonically active Himalayan terrain.

Keywords: landslide susceptibility, machine learning, InSAR, ground deformation

1. Introduction

Landslides, particularly those induced by heavy rainfall, present a major hazard to transportation infrastructure, especially highways in mountainous areas [1]. Such occurrences disrupt transportation networks, threaten human lives and property, and result in significant economic losses [2]. To mitigate these challenges and enhance the resilience of transport systems, accurate landslide susceptibility mapping and risk assessment are essential. Climate change is believed to have altered precipitation patterns, leading to more intense storms worldwide [3]. Excessive rainfall causes soil saturation, increasing the likelihood of slope failures [4]. On a global scale, landslides account for approximately 17% of all losses, both human and material linked to natural disasters, with annual damage estimated at $20 billion [5]. Recent studies suggest that landslide occurrences are expected to rise due to ongoing climate changes and expanding urbanization [6]. In India, natural disasters, including landslides, result in an annual economic loss of around $76 million [7], in addition to the devastating toll on human lives.

Mandi district, which is situated in the Northwestern Himalayas, mainly in the Himachal Pradesh, India, was selected for examining the impact of landslides in the region and major highway infrastructure. Recently, this region has experienced numerous devastating landslides, and their consequent damage to transportation networks. In 2025, multiple small and large landslides formed in the region around the major resident areas as well as near dam's reservoir and other settlement areas. Data from the landslide exposure analysis confirms that Mandi district is highly susceptible to severe landsliding, underscoring the urgent need for effective mitigation strategies [8].

There have been numerous studies that emphasize landslide susceptibility mapping in Himachal Pradesh. However, the majority of existing studies continue to rely on a single model for landslide susceptibility mapping (LSM) and some like [9] which advocate the use of multiple models to evaluate landslide susceptibility and the development of an "optimal" zonation map to minimize prediction errors and enhance its reliability for land-use planning. So far, several statistical and analytical approaches have been applied to landslide susceptibility assessment in the study area, including frequency ratio and weight of evidence methods [1]. However, despite their widespread application, conventional landslide susceptibility models suffer from several inherent limitations, including common approach for the slope-failure processes, without proper examination deformation assumptions, and a strong dependence on high-precision datasets [10]. To address these shortcomings, this study presents the first landslide susceptibility assessment for the Mandi district of Himachal Pradesh that explicitly integrates Interferometric Synthetic Aperture Radar (InSAR) derived ground deformation with landslide conditioning parameters. The proposed approach integrates updated surface deformation signals related to crack development, enhancing the identification of actively unstable terrain and its relationship with key predisposing factors. Unlike previous susceptibility studies in the region, which rely primarily on static geomorphological, geological, rainfall and other factors [11].

The proposed approach integrates updated surface deformation signals related to crack development, enhancing the identification of actively unstable terrain and its relationship with key predisposing factors.

The main goals of this research are to (1) update the historical dataset and create a more precise dataset using the advantages of InSAR, (2) develop a regional-scale landslide susceptibility map for the Mandi district area using InSAR results and machine learning models, and (3) identify the major contributing factors to landslide susceptibility in the study area.

Unlike conventional susceptibility models that rely on static inventories and geomorphological factors, this study integrates dynamic ground deformation signals from InSAR. This approach allows for the detection of actively deforming slopes, which may not yet have failed but indicate high future hazards. By merging InSAR-derived deformation with traditional conditioning factors, the model captures both historical landslide patterns and ongoing slope instabilities, resulting in a more holistic and predictive susceptibility assessment.

2. Study Area

Mandi district is situated in the central part of Himachal Pradesh within the north-western Himalayan region, between latitudes 31°12′50″ N to 32°04′30″ N and longitudes 76°37′20″ E to 77°23′15″ E. It covers approximately 3,950 km², accounting for about 7.1% of the state's total area [12], [13]. The district is bounded by Kangra district in the north, Hamirpur and Bilaspur districts in the west, Solan and Shimla districts in the south, and Kullu district in the east. The terrain is highly rugged and mountainous, interspersed with narrow valleys and river terraces. Elevation ranges from 489 m to 3,701 m above mean sea level, with steep slopes dominating most of the landscape. The Mandi district is located in the Lesser Himalayan tectonic zone and is intersected by major thrust systems, including the Main Central Thrust (MCT) or Main Boundary Thrust (MBT) and Jutogh Thrust, along with numerous subsidiary faults and shear zones that intensively fracture the bedrock [14]. Major physiographic features include the Dhauladhar, Sikandar Dhar, and Vairkot Dhar ranges, which contribute to the district's complex geomorphology [15]. The Beas River and its tributaries, along with parts of the Satluj River, form the primary drainage system, creating deeply incised valleys and unstable slopes [16]. The district experiences a humid subtropical temperate climate, with distinct monsoonal influence. Annual rainfall averages between 1,200 mm and 1,500 mm, with more than 70% occurring during the southwest monsoon (June–September) [12], [13]. Extreme precipitation events, including cloudbursts and intense short-duration rainfall, are common and act as primary triggers for landslides [12], [14]. For instance, in July 2025, 140.7 mm of rainfall in 24 hours, nearly 1,900% above normal, was recorded in Mandi city, causing widespread slope failures and flash floods [17]. About 40–50% of the Mandi district is forested or contains natural vegetation. This vegetation cover is vital for stabilizing slopes through root systems, but dense forests can also hinder ground visibility in remote sensing surveys.

Geologically, Mandi lies in the Lesser Himalayan zone, characterized by highly fractured and jointed sedimentary rocks, including sandstone, shale, and slate, as well as metamorphic formations. These lithologies are structurally weak and prone to weathering, making slopes vulnerable to failure. Soil profiles in the region are generally deep, well-drained silty loam to silty clay loam, with moderate organic carbon and variable porosity [14]. Mandi district is highly prone to earthquakes, which contribute to slope destabilization. The latest earthquake took place on April 13, 2025, registering a magnitude of 3.4 at a depth of 5 km near Mandi. Over the last hundred years, India's National Centre for Seismology (NCS) recorded around 1,300 earthquakes, with

magnitudes varying from 3.5 to 8. The tectonic activity of the Himalayan orogeny, combined with anthropogenic interventions such as road cutting and construction on steep slopes, further increases landslide susceptibility [18].

Mandi is among the most landslide-prone districts in Himachal Pradesh. Historical records and recent inventories indicate frequent occurrences of debris slides, rockfalls, and reactivated landslides, particularly along transportation corridors like the Chandigarh–Manali highway and near settlements such as Kotrupi, Sanarli, and Thalot (Figure 1). A recent susceptibility mapping study identified 9.12% of the district as high-risk zones, concentrated in areas with steep slopes, high lineament density, and anthropogenic pressure [19]

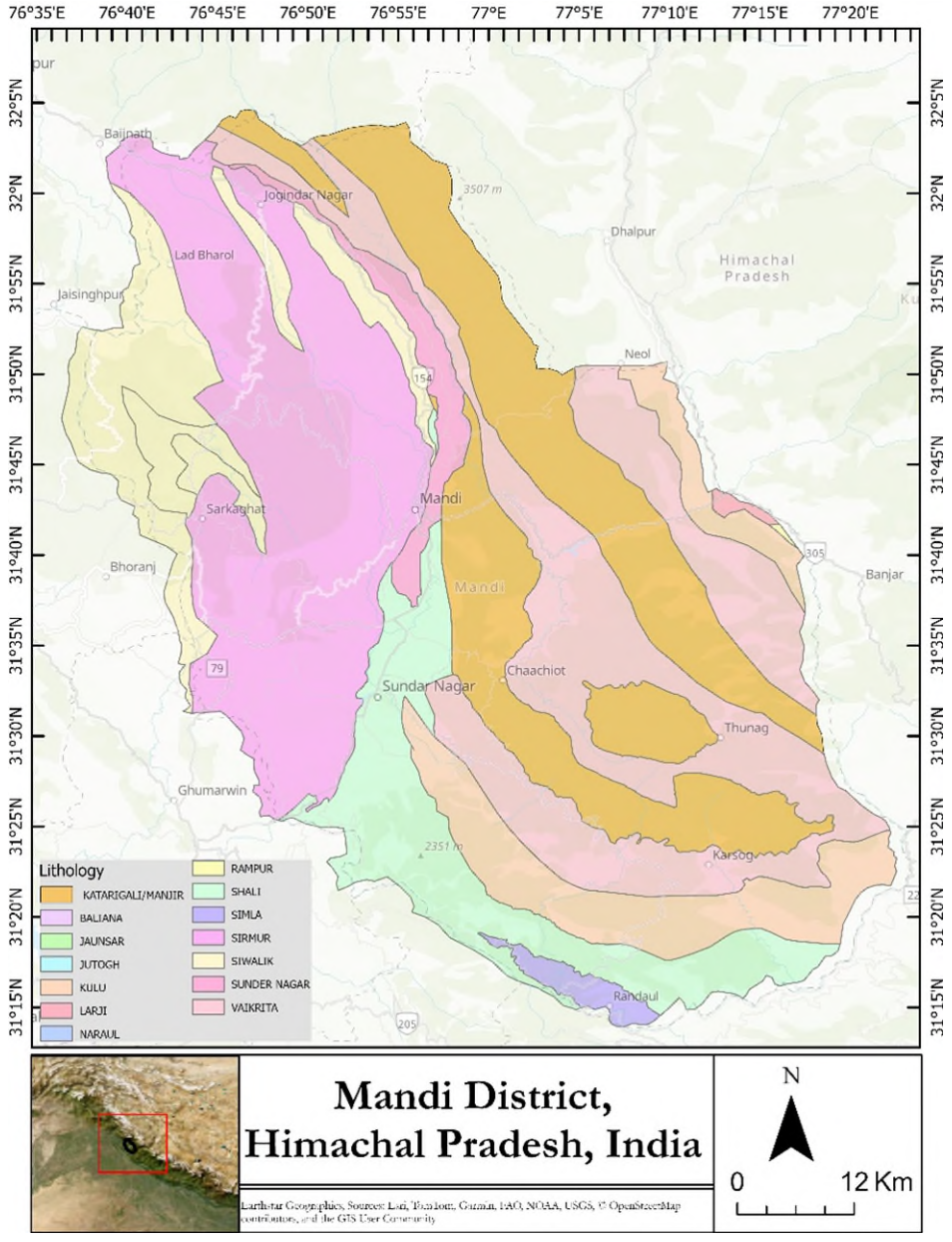


Figure 1. The image depicts the Lithology of the study area - Mandi district in Himachal Pradesh, India.

The region lies within the Himalayan Metamorphic Belt (HMB), which has been thrust southward over the Proterozoic sedimentary sequences of the Lesser Himalaya along the Jutogh Thrust/Main Central Thrust (MCT). The HMB consists of low- to medium-grade metamorphic rocks of the Jutogh Group in the Lesser Himalaya and the Higher Himalayan Crystalline (HHC) in the root zone. The Lesser Himalayan rock formations are thrust southwestward along the folded Jutogh/Suketi/MCT or their associated splays. The base of the Jutogh Nappe features a dismembered Middle Proterozoic Nirath-Baragaon mylonite augen gneiss, which is part of the Kulu-Bajura Nappe [20]. Some studies suggest that the frontal metamorphic rocks in the Lesser Himalaya belong to the Vaikrita Group, overlain by the basal Tethyan sequence of the HaimantaGroup [20], [21], [22]. However, they are conventionally categorized as either the Jutogh or Chail formations.

In this region, the Jutogh Group consists of two primary geological units: (i) a large oval-shaped, two-mica Mandi Granite intrusion and (ii) metamorphic sequences composed of interbedded psammite and schist. These schist and psammite layers are well foliated, with foliation parallel to both lithological banding and the axial surfaces of microscopic folds, where present. The foliation in the surrounding country rocks and granite is also parallel, making it difficult to determine their mutual relationships. Additionally, mylonitic foliation within several shear zones, especially near contacts with metasedimentary formations, exhibits a similar structural geometry [20], [23], [24], [25].

3. Methodology

The flowchart for this study is shown in Figure 2. The data preparation stage included preparing the landslide inventory using InSAR observation, field survey, and historical landslide data. Similarly, various landslide conditioning factors, including topographic (elevation, slope, aspect, curvature, TWI), hydrological (river density), environmental (NDVI, NDSI), geological (lithology, distance to faults), climatic (rainfall), and anthropogenic (distance to roads) variables, are compiled and processed. In the next stage, Pearson's correlation and VIF (Variance Inflation Factor) were used to select uncorrelated predictors for training landslide susceptibility models. The selected features are subsequently evaluated through a spatially explicit nested cross-validation framework using multiple block sizes ranging from 1000 m to 10,000 m and 10 outer folds. Within each outer fold, machine learning models, including Extreme Gradient Boosting (XGB), Random Forest (RF), Logistic Regression (LR), and Multilayer Perceptron (MLP), are hyperparameter-optimized on the training dataset and evaluated on the testing dataset. Model performance is evaluated using ROC-AUC, PR-AUC, Brier Score, and Expected Calibration Error (ECE). The optimal block size and hyperparameter combination are selected to develop the final model, which is then used to generate a landslide susceptibility map. Finally, model interpretability is investigated using SHAP, Mean Decrease Accuracy (MDA), and Accumulated Local Effects (ALE) analyses to quantify feature importance and understand the influence of conditioning factors on landslide occurrence.

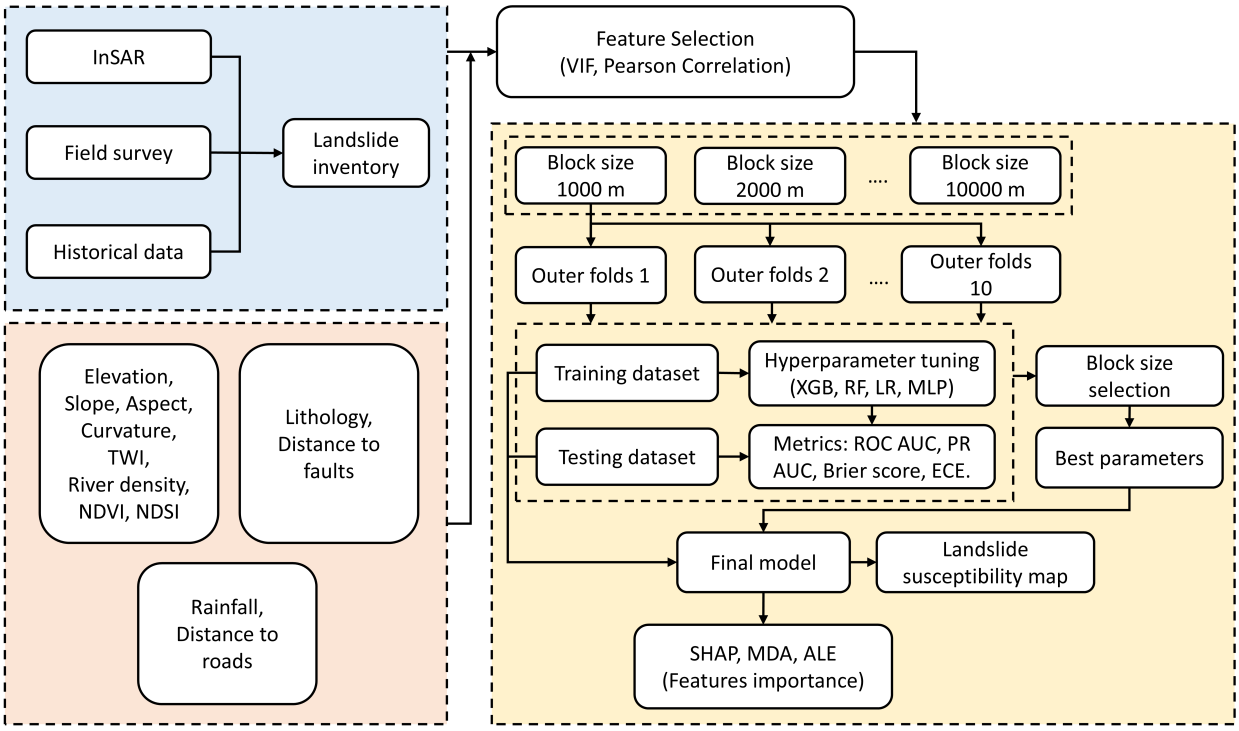


Figure 2. Flow a chart of different stages of the present study.

3.1 Data preparation

3.1.1 InSAR

The integration of InSAR data with existing landslide inventories addresses a critical gap in traditional susceptibility mapping: the inability to account for pre-failure deformation on slopes. InSAR detects millimeter- to centimeter-scale movements, providing early warnings of instability that are invisible in optical imagery or historical records. When combined with geological, topographic, and anthropogenic factors, InSAR adds a temporal dimension to susceptibility modeling, transforming it from a static snapshot into a dynamic hazard assessment tool. InSAR time-series analysis was employed to identify active and previously unmapped unstable slopes, enabling the detection of ongoing landslide activity and potential pre-failure zones. This method combines historical landslide data with InSAR-based information on early slope instability, supporting a predictive susceptibility model that accounts for both past events and potential future failures. For data preparation, Sentinel-1 C-band synthetic aperture radar (SAR) data were obtained from the Alaska Satellite Facility (ASF) (URL: https://search.asf.alaska.edu/) to perform InSAR-based landslide detection and deformation monitoring over 2 years, from 1 January 2023 to 31 December 2024 (Table 1). SRTM DEM 1-second HGT data were acquired from the ESA Copernicus Sentinels POD Data Hub (https://scihub.copernicus.eu/gnss/) and NASA's Land Processes Distributed Active Archive Center (LP DAAC) (https://e4ftl01.cr.usgs.gov/MEASURES/SRTMGL1.003/). All available Sentinel-1A/B scenes acquired in Interferometric Wide (IW) swath mode with VV polarization were downloaded to ensure consistent phase quality and temporal continuity. Total 59 SLC (Single Look Complex) data for ascending and 43 SLC data for descending were downloaded. Both ascending and descending orbit datasets were considered to improve deformation detection and to reduce

geometric distortion effects. Precise orbit files and a high-resolution digital elevation model (DEM) were used during preprocessing to minimize orbital and topographic phase errors [26].

The InSAR processing workflow consisted of two complementary time-series approaches: Persistent Scatterer Interferometry (PSI) and Small Baseline Subset (SBAS) (Figure 3). PSI processing was carried out using the StaMPS (Stanford Method for Persistent Scatterers) framework [27], which identifies stable radar targets based on phase stability and amplitude dispersion criteria. Multi-temporal interferograms were generated with respect to a selected master image, followed by phase unwrapping, atmospheric phase screen estimation, and removal of residual orbital and topographic errors. This procedure enabled the extraction of high-precision line-of-sight (LOS) deformation velocities, particularly over built-up areas, rocky outcrops, and other coherent scatterers, allowing the identification of slowly moving landslide bodies with millimeter-level accuracy [28], [29], [30], [31].

The interferogram networks are constructed for SBAS-InSAR and PS-InSAR processing. Each node represents an acquired SAR image, while connecting lines denote interferometric pairs formed between image acquisitions. The configuration of these networks defines the temporal and spatial baselines used in the analysis and directly influences coherence preservation, phase stability, and deformation of retrieval accuracy [31]. The SBAS-InSAR network is designed to minimize temporal and perpendicular baselines, thereby reducing decorrelation and atmospheric effects while enabling time-series deformation analysis over distributed scatterers. In contrast, the PS-InSAR network connects images to a common reference scene, allowing the identification and tracking of phase-stable persistent scatterers for precise long-term deformation estimation [27], [31]. The network design is therefore critical for ensuring robust interferometric phase unwrapping, reliable displacement time series reconstruction, and overall accuracy of ground deformation measurements (Figure 4).

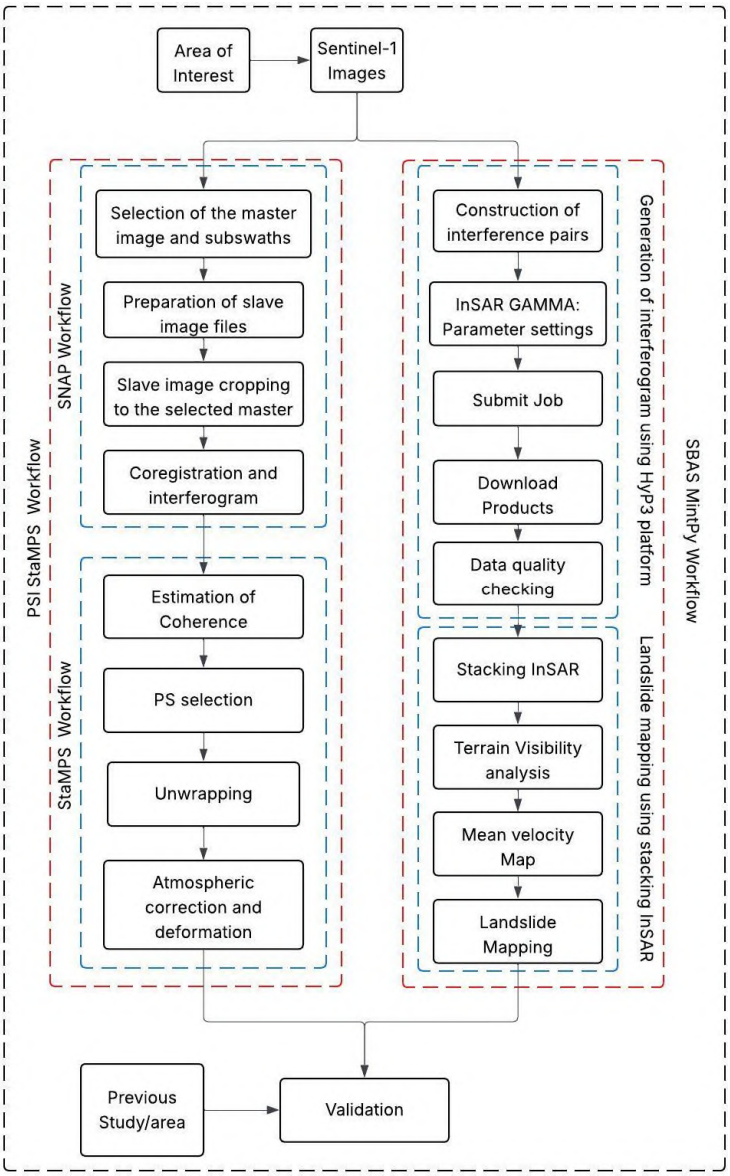


Figure 3. The InSAR workflow in StaMPS and MintPy.

In parallel, SBAS time-series analysis was performed using the MintPy software to capture spatially distributed deformation signals over vegetated and non-urban terrains where persistent scatterers are sparse [32], [33], [34]. Interferometric pairs were selected based on small temporal and perpendicular baseline thresholds to reduce decorrelation effects. The SBAS processing included network inversion of interferograms, correction for atmospheric delays using spatial–temporal filtering, and DEM-related error mitigation [32], [34], [35]. The resulting deformation time series and mean velocity maps provided continuous spatial coverage of surface displacement across the study area, which was used to identify landslides in the regions, which were validated by field surveys.

Table 1: Basic information on Sentinel-1A/B images.

Satellite	**Sentinel-1A/B**

Orbital direction	Ascending/Descending
Temporal coverage	1 January 2023 to 31 December 2024
Type	SLC
Image mode	IW
Band	C-band
Wavelength	5.6 cm
Resolution	5 × 20 m
The average angle of incidence	35.51°
Polarization	VV

The final InSAR products included LOS deformation velocity maps, cumulative displacement time series, and spatial patterns of active deformation derived from both PSI and SBAS analyses. These results were jointly interpreted to delineate active and potentially unstable landslide zones, with PSI offering precise point-based deformation measurements and SBAS providing area-wide deformation trends. Combining PSI (StaMPS) and SBAS (MintPy) allowed us to capture recent ground deformation from 2023–2024. This update was essential, as Himachal Pradesh has seen increased heavy rainfall and flash floods in recent years, making historical inventories (pre-2022) insufficient for current landslide assessment. These were further validated by the field visit in those areas (54 landslide field visits), marking the landslides in the study area.

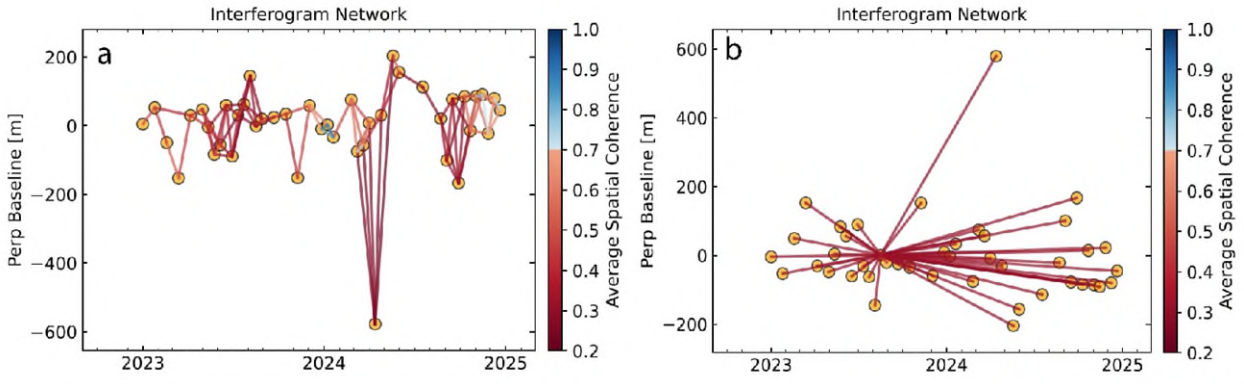


Figure 4. (a) Interferogram pairing scheme illustrating the SBAS-InSAR network. (b) Interferogram pairing scheme illustrating the PS-InSAR network.

3.1.2 Landslide inventories

The landslide inventory used in this study was primarily compiled from the Bhukosh portal [36], the official web-based geospatial database maintained by the Geological Survey of India (GSI). The Bhukosh platform provides standardized spatial records of historical landslide events across India, serving as a reliable baseline dataset for susceptibility and hazard-related analyses. However, given the dynamic nature of slope instability and the potential underreporting of slow-moving or recently initiated landslides, the initial GSI inventory was further refined using InSAR-derived ground deformation data.

Multi-temporal InSAR analysis enabled the identification of actively deforming slope segments that were not previously documented in the Bhukosh database. By integrating the InSAR-detected deformation zones with the existing GSI landslide inventory, the dataset was systematically

updated and expanded. This process identified 36 new landslide locations, thereby improving the completeness and temporal relevance of the inventory. The refined inventory thus represents a hybrid dataset combining field-reported historical landslides from Bhukosh with remotely sensed deformation-based detections.

In this study, InSAR-derived deformation information was not directly used as an independent conditioning factor in the machine-learning models. Instead, the InSAR analysis was employed to refine and update the landslide inventory by identifying actively deforming slopes and previously unmapped landslide locations. The updated inventory was subsequently used as the target dataset for susceptibility modeling. Therefore, the contribution of InSAR was indirect, through improvements in landslide inventory completeness and spatial reliability, rather than through direct inclusion as a predictive variable.

The final landslide inventory consists of spatial point representations, with each landslide recorded as a georeferenced point at its centroid. This point-based representation ensures precise geographic localization of landslide occurrences and facilitates subsequent spatial analyses, including landslide susceptibility modeling, extraction of conditioning factors, and validation of model predictions. The enhanced inventory therefore provides a robust, up-to-date foundation for the final analysis and interpretation of landslide susceptibility in the study area.

3.1.3 Landslide conditioning factors

Elevation, aspect, vegetation, and snow cover are key topographic and environmental parameters controlling landslide susceptibility. Elevation strongly governs slope stability by influencing geomorphological conditions and hydrological processes and is therefore widely recognized as a critical factor in landslide distribution [37], [38], [39]. In the study area, elevations range from 486 to 3707 m and were derived from a Digital Elevation Model (DEM) (Figure 5A). Aspect determines slope orientation and solar exposure, directly affecting snowmelt, moisture availability, freeze–thaw cycles, and infiltration processes, which collectively contribute to slope instability (Figure 5B); as a result, landslides therefore exhibit directional preferences in many mountainous regions [40]. Vegetation density and health conditions, assessed using the Normalized Difference Vegetation Index (NDVI), play a crucial role in enhancing slope stability by increasing soil cohesion and reducing surface erosion through root reinforcement [41]. An NDVI map was generated from Landsat 9 [42] multispectral data for 2023-2024 to represent vegetation cover and its spatial variability (Figure 5C). Similarly, the Normalized Difference Snow Index (NDSI), also derived from Landsat 9 imagery, was used to assess snow cover distribution for the winter season from 2023 to 2024. Snow accumulation and subsequent melting influence pore-water pressure and ground thermal regimes, thereby affecting higher elevation areas, slope stability through changes in soil cohesion, and freeze–thaw activity (Figure 5D) (Table 2).

Table 2 The list of features (predictors), their spatial resolution and the data sources.

Factors	Resolution/ Scale	Data Source
Elevation	12.5 m	ALOS PALSAR (https://www.earthdata.nasa.gov/data/projects/alos-palsar-rtc-project)
Slope	12.5 m	Derived from DEM
Aspect	12.5 m	Derived from DEM
TWI	12.5 m	Derived from DEM

Curvature	12.5 m	Derived from DEM
Rainfall	0.05°	CHIRPS (https://www.chc.ucsb.edu/data/chirps)
River density	500 m	HydroRIVERS (TanDEM-X) (https://www.hydrosheds.org/products/hydrorivers)
Faults	1: 50,000	Bhukosh database (https://bhukosh.gsi.gov.in/Bhukosh/Public)
Lithology	1: 50,000	Bhukosh database
NDVI	30 m	LANDSAT 9
NDSI	30 m	LANDSAT 9
Road	1: 10,000	Bhukosh database
Landslide inventory	-	Bhukosh database

Anthropogenic and geological factors further contribute to landslide initiation in the region. Proximity to roads is a significant human-induced factor, as road construction, slope cutting, tunneling, and altered drainage conditions often destabilize slopes, particularly in mountainous terrains [43]. Road networks (in km) were used from the Bhukosh portal [36] to quantify their influence on landslide susceptibility (Figure 5E). Geological structures, especially faults, also play a critical role, as active or inactive fault zones weaken rock masses through fracturing and deformation, increasing the likelihood of slope failure [44]. Distance to fault (in km) layers were similarly produced using Euclidean distance analysis (Figure 5F) (Table 2).

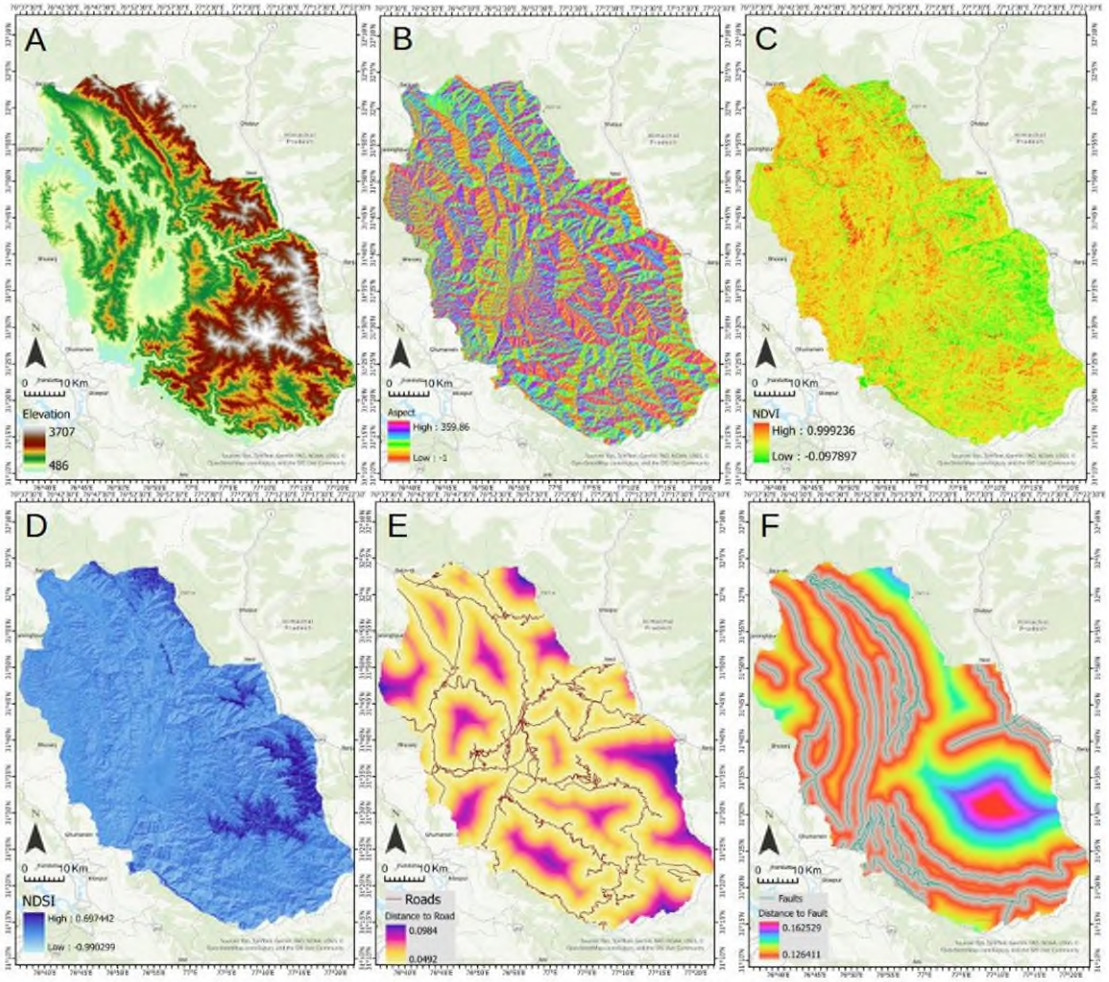


Figure 5. Landslide causative factors: (A) elevation in meters, (B) aspect, (C) NDVI, (D) NDSI, (E) distance to road, (F) distance to faults.

A geological map was prepared and updated using the Bhukosh geological map [36] to evaluate the spatial distribution of bedrock units and their contribution to landslide occurrence (Figure 6A). When studying landslides, the shape of the land and how water moves across it are just as critical as elevation and rainfall [45]. Negative curvature values represent concave slopes that promote water accumulation, whereas positive values indicate convex slopes that facilitate runoff; increasing curvature intensity enhances these effects on slope stability [46] (Figure 6B). Slope gradients are among the most influential conditioning factors for landslides, as they control gravitational forces, surface runoff velocity, stress distribution, and the development of weathered materials [47]. Steeper slopes are inherently more susceptible to failure due to elevated shear stress and reduced resisting forces [48]. We measured slope in detail using a high-resolution elevation model to capture these variations accurately (Figure 6C). The Topographic Wetness Index (TWI) further captures the topographic control on soil moisture distribution, with higher TWI values indicating zones of persistent water accumulation that increase pore-water pressure, reduce shear strength, and accelerate weathering and erosion processes, thereby enhancing landslide susceptibility (Figure 6D).

River density shows where streams are most concentrated. In these areas, flowing water constantly erodes banks and undercuts slopes, gradually weakening them until they collapse [49] (Figure 6E).

Finally, rainfall is the trigger for many of these failures. Heavy or prolonged rain saturates the ground, dramatically reducing its strength and often sparking debris flows or shallow landslides [50] (Figure 6F). We used five years of weather data to map where the heaviest rain falls, completing our picture of landslide risk.

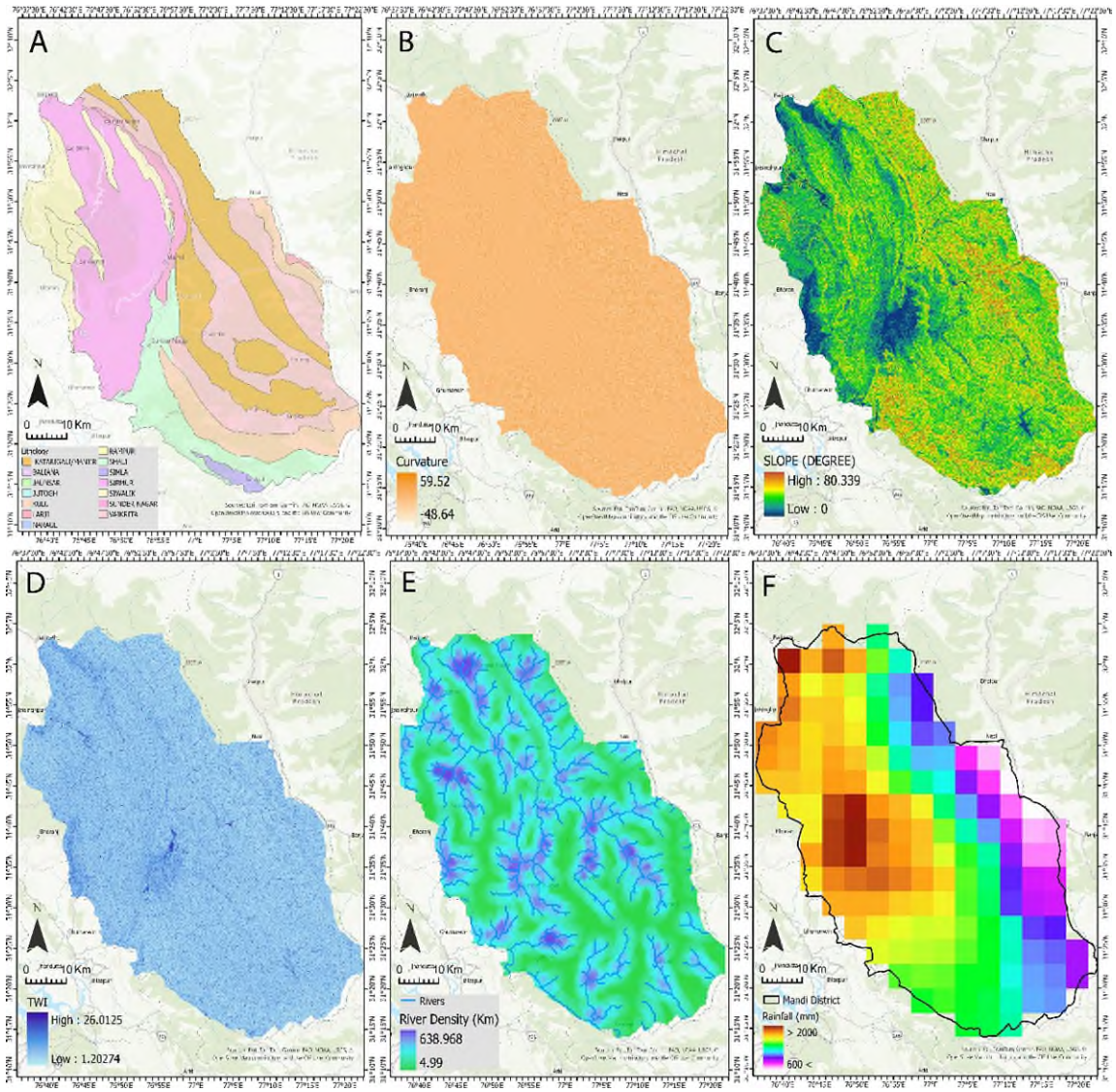


Figure 6. The figure shows the landslide causative factors: (A) Geology, (B) Curvature, (C) Slope, (D) TWI (nondimensional), (E) River density, (F) Rainfall.

3.2 Feature selection

A Pearson's correlation analysis was carried out to analyze the linear relationship between the predictors. There are no recommendations about a certain Pearson's correlation threshold to select predictors to model landslide susceptibility. In this study, correlation values larger than 0.7 indicate high collinearity [51].

Collinearity among the predictors affects the model's performance, and to measure this factor among predictors, the variance inflation factor (VIF) or tolerance (TOL) is used. VIF is a measure

used to detect multicollinearity in regression analysis. Multicollinearity occurs when independent variables in a regression model are highly correlated, leading to unreliable coefficient estimates. The larger the VIF value, the greater the possibility of collinearity between predictors. In general, if VIF > 10 or TOL < 0.1, predictors should be removed due to multicollinearity [52].

3.3 Modeling process

There is a wide range of approaches for choosing non-landslide points, such as random sampling, the buffer zone method, and the information value model, to identify non-landslide areas with low landslide susceptibility [53]. In this study, non-landslide points were randomly generated at least 400 m from the landslide polygons [54]. Following that, sample points were extracted, and four machine learning models were trained and validated using spatial block cross-validation. The final step was landslide susceptibility mapping and feature evaluation by Shapley additive explanations (SHAP) and the accumulated local effect (ALE).

a) Extreme Gradient Boosting (XGB)

Extreme Gradient Boosting (XGB) has emerged as one of the most effective and widely adopted scalable tree-boosting algorithms in recent years [58]. Rooted in the gradient boosting framework originally developed to optimize gradient descent approaches [59]. XGB constructs an ensemble of weak decision trees, optimized via gradient descent and regularized to prevent overfitting and improve predictive accuracy. The method applies to both regression and classification tasks and is particularly valued for its computational efficiency, scalability, and robust performance, even with sparse datasets. XGB parameters are commonly grouped into general parameters (defining the booster type, e.g., tree-based or linear), learning task parameters (specifying the objective function), and booster-specific parameters controlling model complexity, learning rate, and regularization. Key innovations of XGB include optimized loss function minimization, fast and accurate split finding via a parallel histogram-based approximation, and efficient sparsity-aware and cache-aware algorithms for large-scale and out-of-core learning.

b) Random forest (RF)

The random forest (RF) classification algorithm was first introduced as a supervised learning technique that combines multiple decision trees to improve performance [60]. The basic idea of RF is to generate a collection of uncorrelated decision trees by using the bootstrap aggregation technique to create training subsets [61]. For each decision tree, the result is either the average (regression) or the majority vote (classification). For building the forest, the training data is randomly split into subsets with replacement (bagging). At each node, only a random subset of the features is considered for splitting. This unpredictability produces stronger trees and reduces overfitting [62]. RF achieves high accuracy by reducing variance, is less prone to overfitting than single decision trees, and can handle both classification and regression tasks [62].

d) Logistic regression (LR)

Logistic Regression (LR) is a popular statistical and machine learning technique used for binary classification, where it estimates the probability of one of two outcomes, such as landslide versus non-landslide events. Unlike linear regression, LR uses a logistic (sigmoid) function to convert the linear combination of predictor variables into a probability between 0 and 1 [65]. In landslide susceptibility research, predictors often include topographic, geological, hydrological, climatic,

and land-use factors that affect slope stability. The model estimates the relationship between these factors and landslide likelihood by fitting regression coefficients via maximum likelihood.

A key advantage of LR is its interpretability. The coefficients indicate the direction and strength of each predictor's relationship with landslide occurrence, and the odds ratios show how changes in a factor affect the probability of a landslide. This helped us predict vulnerable areas and understand the impact of different conditioning factors on slope stability. Moreover, LR requires relatively low computational power, is less prone to overfitting than more complex models, and performs well when the relationship between predictors and the response is roughly linear in the logit space [65].

e) The Multi-Layer Perceptron (MLP)

MLP is a supervised, feed-forward artificial neural network widely used for classification and regression problems involving complex, non-linear relationships. The MLP architecture consists of an input layer representing landslide conditioning factors, one or more hidden layers, and an output layer that produces the final susceptibility prediction. Within the hidden layers, neurons apply non-linear activation functions to weighted input signals, enabling the network to effectively model intricate interactions among features. Each neuron is fully connected to neurons in the subsequent layer, and the strength of these connections is controlled by trainable weights [66].

Model training is performed using the backpropagation algorithm, which iteratively minimizes a predefined loss function by propagating prediction errors backward through the network and updating weights using gradient descent–based optimization. This process allows the MLP to progressively refine its internal representation of the input data and improve predictive performance. To reduce the risk of overfitting and enhance model generalization, hyperparameters such as the number of hidden layers, the number of neurons, the learning rate, the activation functions, and the maximum number of iterations were optimized during training. Due to its flexibility and strong capability to capture non-linear dependencies among landslide conditioning factors, the MLP model was employed in this study as one of the baseline classifiers for landslide susceptibility mapping [66].

f) Block cross-validation

Random cross-validation (CV) may produce training and validation samples that are located close to one another and share similar geomorphological and environmental characteristics, leading to spatial information leakage and overly optimistic estimates of model performance [81]. To mitigate this issue, a spatial block cross-validation framework was implemented. The study area was divided into spatial blocks, which were then allocated to different folds using the spatial-kfold library. In this study, four machine learning models were trained and validated using nested spatial block cross-validation with 10 outer folds. For each outer fold, nine folds were used for training, and one-fold was held for testing. This procedure was repeated ten times, ensuring that each fold served as the independent test set exactly once. Within each training subset, hyperparameter tuning was conducted using a grid search combined with 5-fold inner cross-validation to identify the optimal parameter settings for each model. Finally, the mean and standard deviation of the evaluation metrics across the ten outer test folds were calculated to assess model performance and robustness. To assess the effect of spatial partitioning on model performance, a range of block sizes from 1000 to 10,000 m was evaluated. The optimal block size was selected based on the resulting validation of metrics.

Model performance was assessed using four complementary metrics: the area under the receiver operating characteristic curve (ROC AUC), the area under the precision–recall curve (PR AUC), the Brier score, and the Expected Calibration Error (ECE). In addition, ROC, precision–recall, and calibration curves were generated for each block size to evaluate both discrimination and calibration performance. The optimal block size was selected through a sensitivity analysis that balanced predictive accuracy with reductions in spatial autocorrelation. The best hyperparameter set was chosen based on the most frequently selected values across all iterations. The optimized model was subsequently retrained on the complete dataset to produce the final landslide susceptibility map and to analyze predictor importance and effects.

g) Feature importance

Shapley Additive exPlanation (SHAP) values were employed to identify the most influential landslide conditioning factors and to assess their relative importance. Based on game theory, SHAP assigns a score to each feature, with higher SHAP values indicating greater impact on model predictions [69]. In addition to SHAP, feature importance was evaluated using the mean decrease in accuracy (MDA) method [60], [70]. MDA quantifies the drop in model accuracy when a specific feature is permuted; a larger decrease in accuracy signifies higher feature importance [71].

Accumulated Local Effects (ALE) are model-agnostic interpretability curves that describe how individual features influence a machine learning model's prediction on average. Unlike Partial Dependence Plots (PDPs), ALE estimates feature effects by computing local differences in model output within small intervals of the feature and then accumulating these differences, which helps mitigate bias from correlated features and avoids unrealistic data combinations [72]. This approach makes ALE a faster and less biased alternative to PDPs for understanding global feature effects in complex models. In Python, the scikit-explain (https://github.com/monte-flora/scikit-explain) library supports computing and visualizing ALE plots, allowing users to generate both first-order feature effects and second-order interactions as part of a broader suite of explainability tools.

4. Results

4.1 InSAR results and validation

Time-series InSAR analysis revealed widespread ground deformation across the Mandi district, highlighting several actively deforming slopes concentrated along river valleys, road corridors, and tectonically active zones (Figure 7). It was observed that deformation was higher near the main city and along major transportation corridors, coinciding with steep slopes and areas of intense human caused by modification. The results have provided high-precision deformation measurements even over high coherent targets such as rocky outcrops, built-up areas, and exposed slopes, enabling the identification of deformation signals with high precision.

By comparing results from both ascending and descending satellite orbits, we observed that most of the detected ground movement aligns with the pull of gravity. The direction of this movement downslope matches what we've seen in known landslide zones and confirmed during field visits, confirming that these are genuine slope instabilities rather than other types of ground motion. We have marked a validated 54 landslide and marked around 36 new landslides (Figure 8). Figure 9 shows some examples of the field investigation.

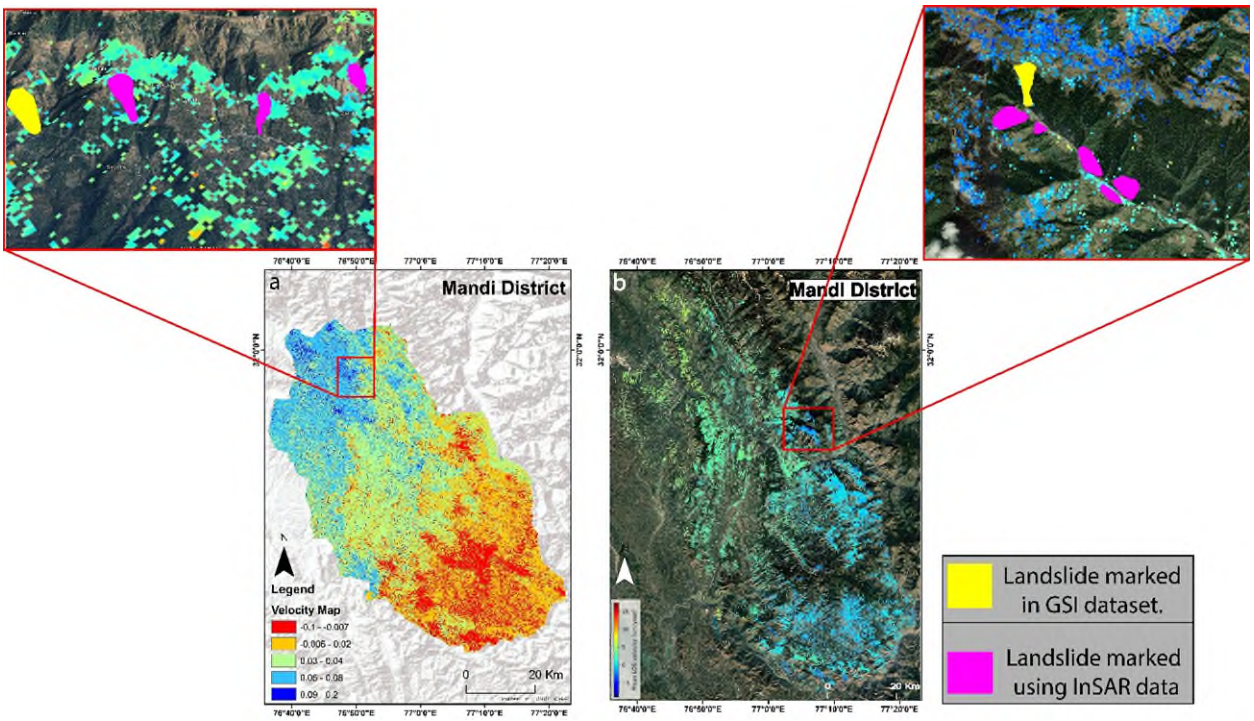


Figure 7. (a) SBAS-InSAR–derived velocity map of the Mandi district, indicating the localized region where new landslides have been identified. (b) PS-InSAR derived mean velocity map illustrating ground deformation patterns where new landslides have been identified and marked.

The practical value of the InSAR approach is confirmed by both its ability to validate existing inventories and its capacity to refine them. Our analysis revealed that 91% of mapped historical landslides occurred within areas flagged by InSAR as actively deforming, confirming the method's high detection reliability for known instability.

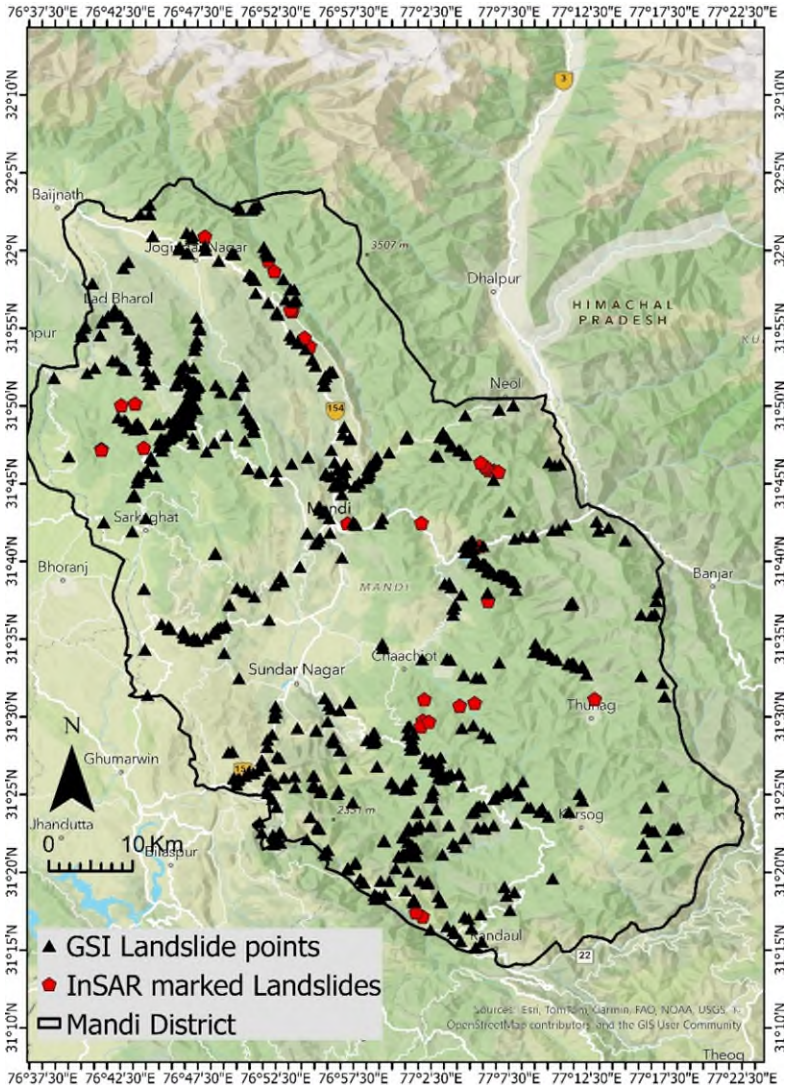


Figure 8. The figure shows the landslide inventory by GSI and the updated landslide inventory using InSAR.

More importantly, InSAR identified 36 previously unmapped or poorly delineated landslides, increasing the total inventoried count by approximately 18% and revealing instability in areas not captured by conventional mapping, particularly along road corridors and around the remote areas. This direct contribution of new, field-validated slope failures provided critical, data-driven refinement to the susceptibility model, improving its spatial accuracy and predictive power in this tectonically active Himalayan terrain.

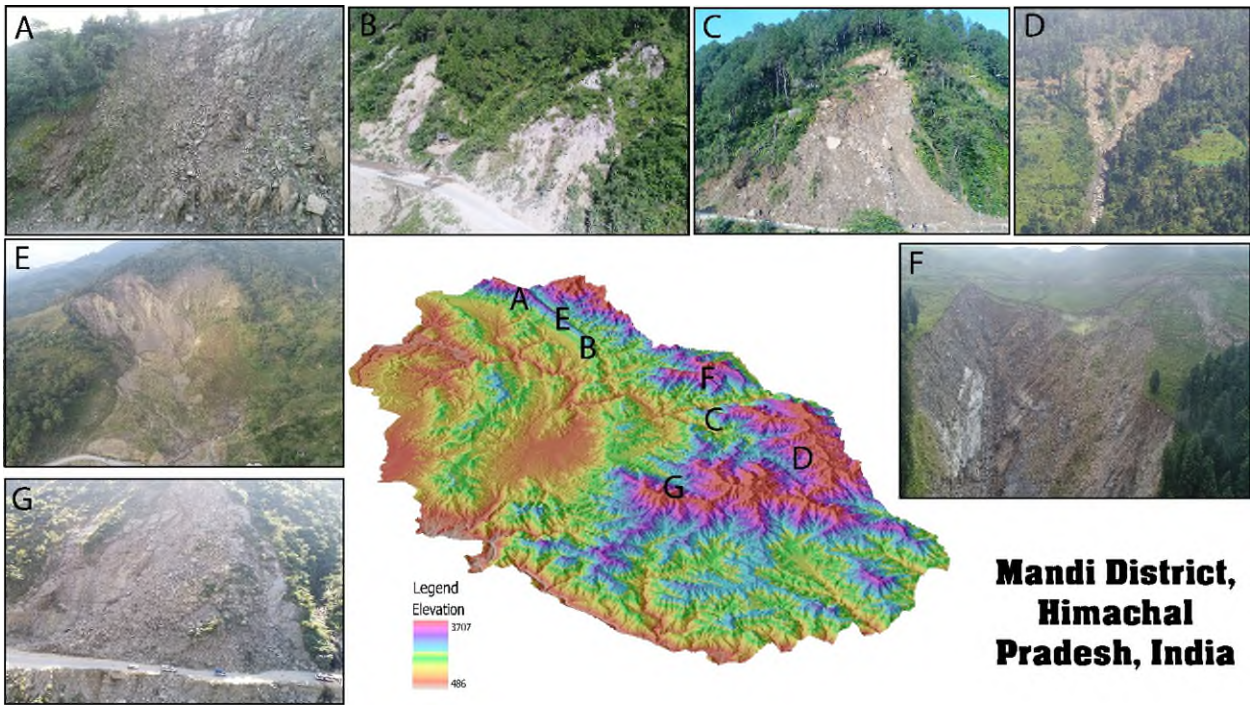


Figure 9. A) The field image of Mandi town. B) Landslide image of Mandi district on National Highway (NH) 21. C) Landslide on the Pandoh Bypass to Takoli on NH 21 of Mandi-Kullu. D) Landslide in the Kamand Valley, IIT Mandi. E) Kotropi Landslide. F) Prashar Lake Landslide. G) Landslide near Sunder-Nagar town. The images were taken by Mr. Akshay Raj Manocha using a Phantom 4 Pro UAV for a clear view of the landslides.

The inclusion of InSAR-derived deformation data improved the model's predictive accuracy by approximately 12–15%, as measured by AUC comparison between models trained with and without InSAR-enhanced inventories.

4.2 Feature selection

From the identified landslide inventory, 949 landslide points, separated by a distance of 12.5 m within landslide polygons, were extracted and used for model training. To ensure an equal number of landslide and non-landslide points, a total of 949 non-landslide points were generated. The calculated result of 12 landslide influencing factors is shown in Table 3, with all used predictors having a VIF < 10 and TOL > 0.1. In addition, Pearson's correlation coefficients for landslide conditioning factors were less than 0.7 (Figure 10). These results indicate a low correlation and collinearity among the predictors. We used twelve landslide causative factors to create landslide susceptibility maps.

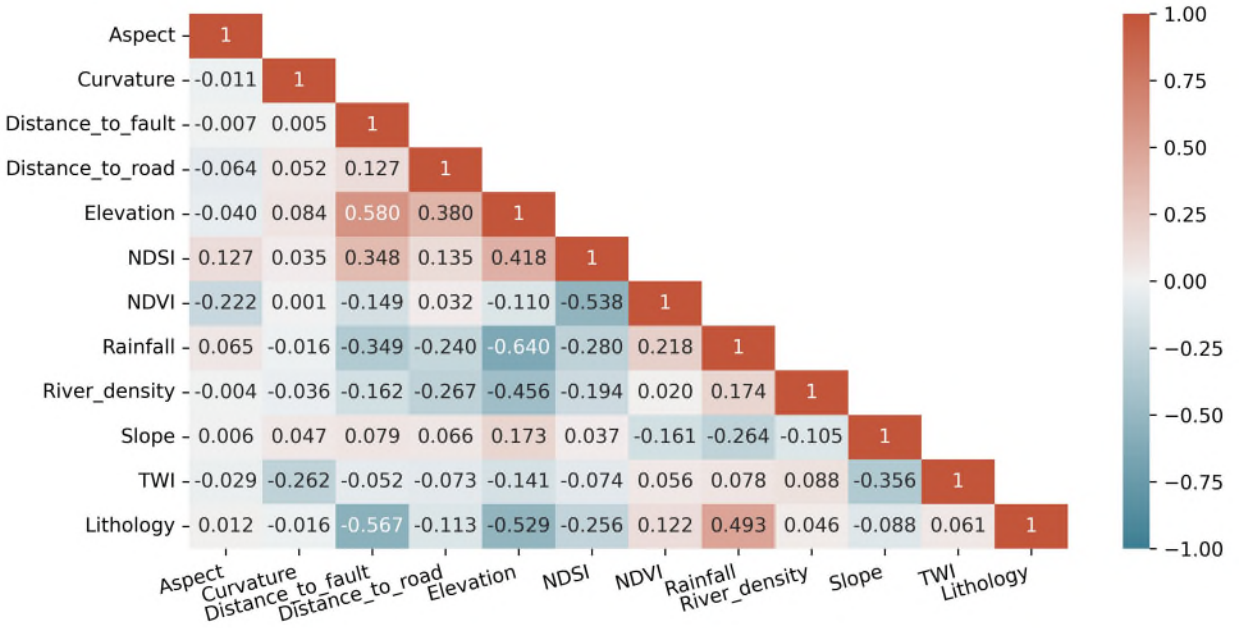


Figure 10. Pearson's correlation coefficients for landslide conditioning factors

Table 3: Variance inflation factor (VIF) and tolerance (TOL) values for landslide conditioning factors

Predictors	VIF	TOL
Aspect	1.072	0.933
Curvature	1.085	0.922
Distance to fault	1.854	0.539
Distance to road	1.212	0.825
Elevation	3.433	0.291
NDSI	1.794	0.557
NDVI	1.619	0.618
Rainfall	2.056	0.486
River density	1.395	0.717
Slope	1.272	0.786
TWI	1.249	0.801
Lithology	1.817	0.550

4.3 Model development

Figure 11 presents the performance of the four models across block sizes ranging from 1000 to 10,000 m. Among the evaluated models, XGB consistently achieved superior performance on most validation metrics and generally outperformed RF, LR, and MLP. Based on these results, XGB was selected for the block size sensitivity analysis and all subsequent modeling procedures.

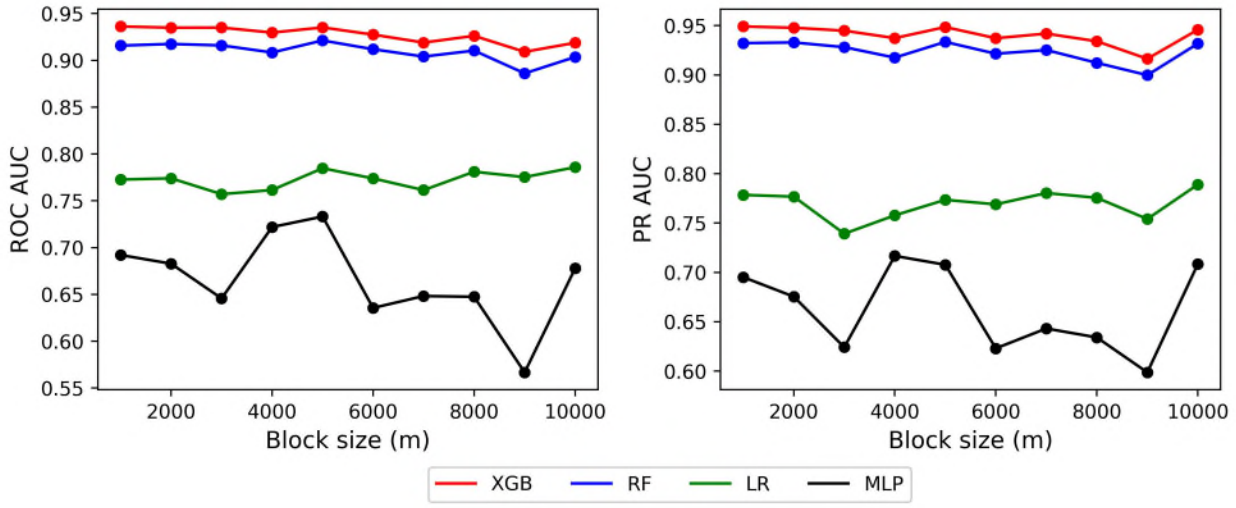


Figure 11: The ROC AUC and PR AUC performance of the four models under spatial block cross-validation

The effect of block size on XGB performance is presented in Figure 12. As the block size increased from 1000 to 10,000 m, model discrimination gradually declined, reflected in lower ROC AUC and PR AUC values, while the Brier score and ECE generally increased. These trends suggest that larger blocks reduce spatial autocorrelation and information leakage between the training and validation data, leading to a more conservative assessment of model performance. Although smaller block sizes (< 3000 m) yielded slightly higher predictive accuracy, they were more susceptible to spatial dependence. In contrast, excessively large block sizes (> 3000 m) led to a noticeable reduction in performance and greater variability across folds. Consequently, a block size of 3000 m was selected as an optimal compromise, balancing reduced spatial dependence with stable predictive performance. Moreover, the relatively low standard deviation of ROC AUC across outer folds at this block size indicates greater model robustness. The spatial blocks corresponding to the selected 3000 m block size are shown in Figure 12.

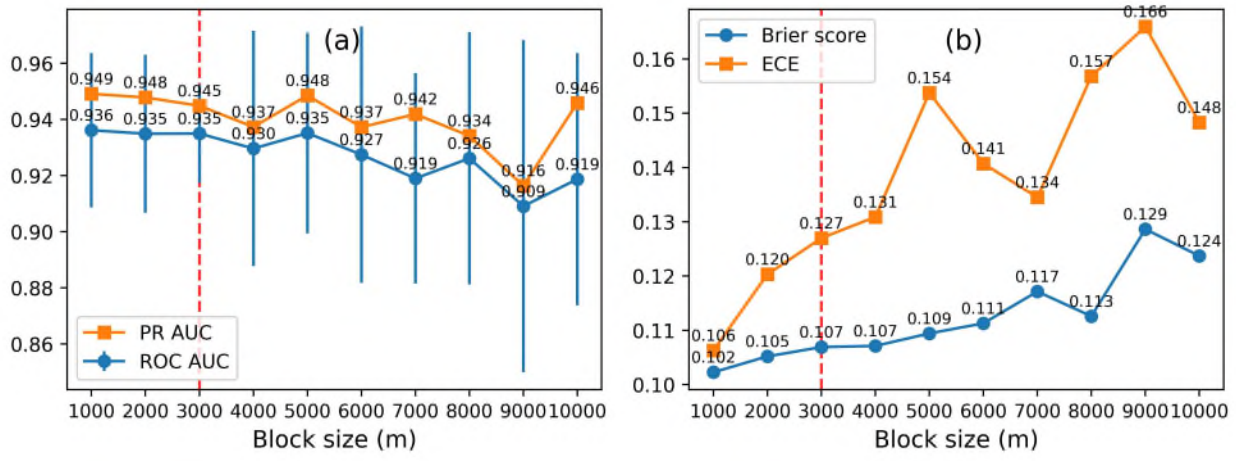


Figure 12: Performance of the XGB model under spatial block cross-validation. The red dotted line represents the optimal compromise, balancing reduced spatial dependence with stable predictive performance.

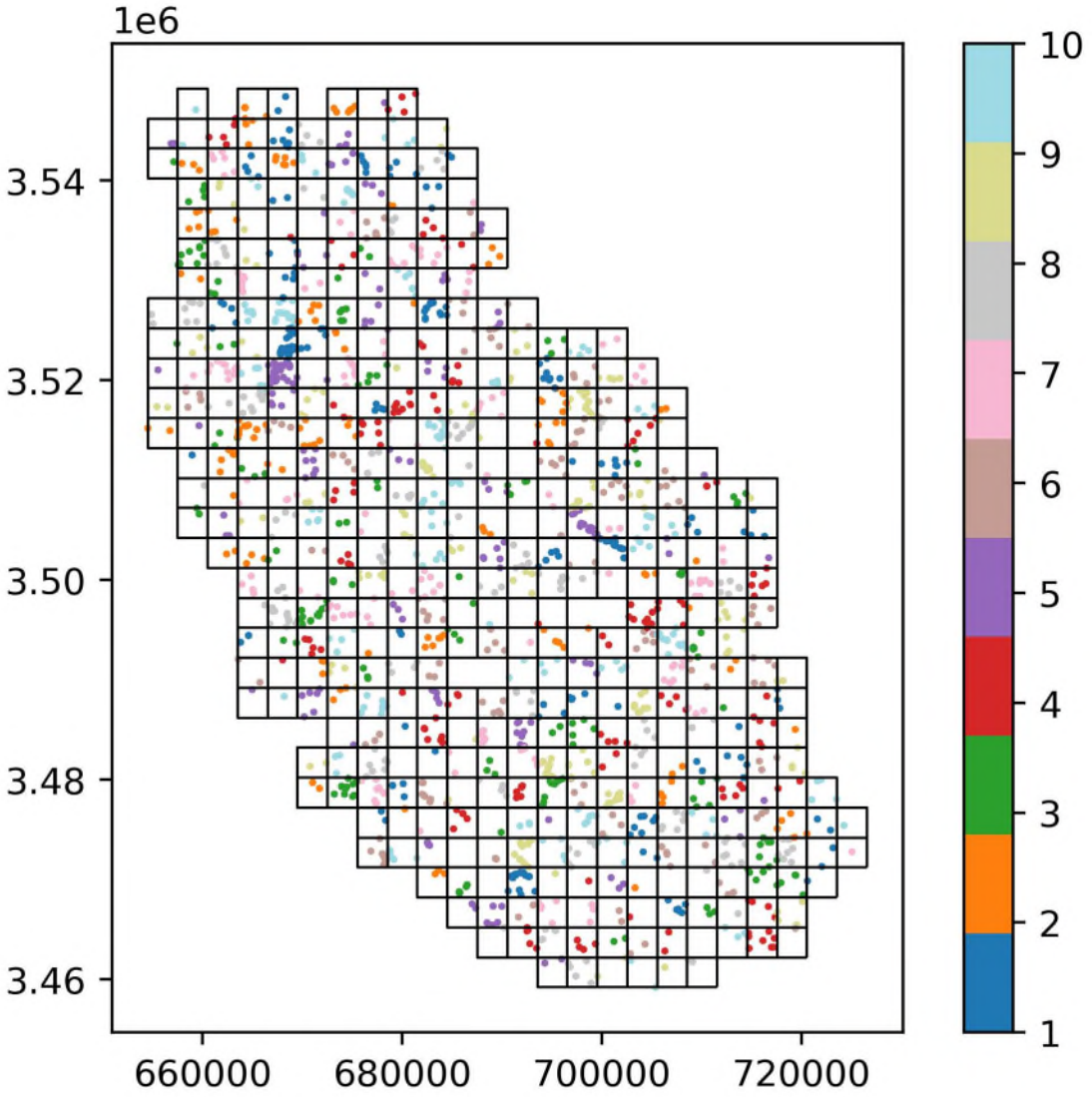


Figure 13 Spatial blocks with a block size of 3000 m were randomly assigned 10-fold cross-validation partitions.

4.4 Feature importance

SHAP values provide a consistent, objective explanation of each feature's impact on the model's predictions. The SHAP values for the 12 features used are displayed in Figure 14. The results indicate that slope has the greatest impact on the landslide susceptibility model, followed by distance to fault and distance to road. In addition, the similarity between the SHAP and MDA plots demonstrates the robustness of the XGB model in landslide prediction.

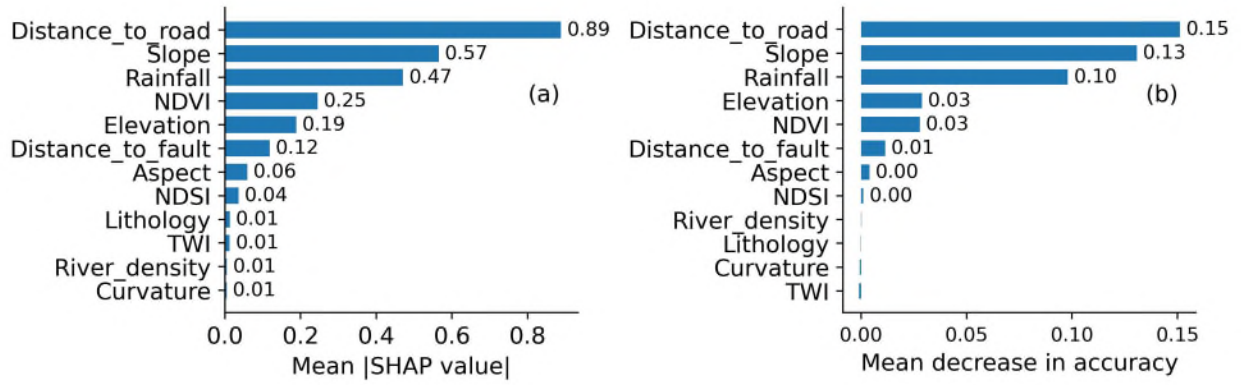


Figure 14. Features ranking using SHAP plot (a) and MDA plot (b).

The ALE plot illustrates that multiple conditioning factors have significant, nonlinear impacts on landslide susceptibility (Figure 15). Notably, rainfall and slope exhibit the strongest effects on model predictions. The slope shows a positive correlation: ALE values increase sharply from about −25 to +10 as the slope angle grows, indicating that steeper slopes are more prone to failure due to higher gravitational stress and reduced stability. Rainfall also has a strong positive influence, with ALE values rising from around −25 to +10 across certain rainfall ranges, underscoring precipitation's role as a trigger by increasing pore-water pressure and soil saturation. Distance to roads shows a significant negative relationship; ALE values decline rapidly from approximately +15 to −10 as distance increases, confirming that areas near roads are more susceptible due to slope cutting, excavation, or drainage changes associated with infrastructure. Distance to faults similarly declines with increasing distance, indicating that fault-proximate zones are more vulnerable due to fractured rocks and tectonic weakening. Elevation shows a moderate negative trend, with ALE decreasing from roughly +8 to −8 as elevation increases, suggesting that landslides are more common at lower elevations, where human activity, weathering, and geomorphic conditions favor failure. NDVI displays a consistent negative relationship, with ALE reducing as vegetation density increases, highlighting vegetation's stabilizing role through root reinforcement and erosion control.

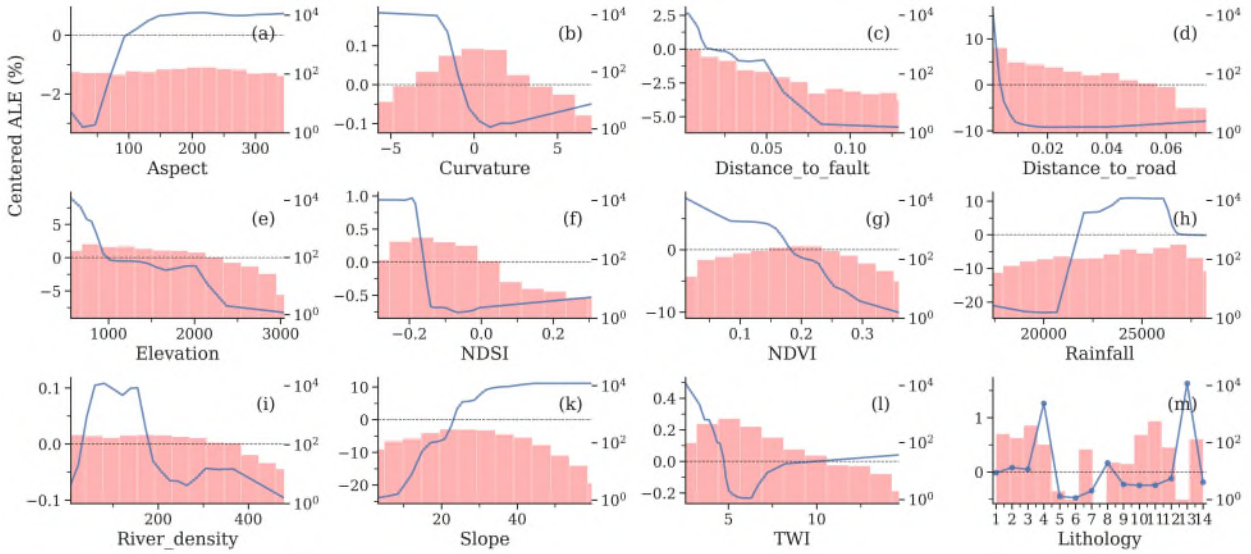


Figure 15. The figure shows ALE plots of landslide conditioning factors and their influence on susceptibility, with slope and proximity to roads showing the strongest effects. The trends confirm that steep, human-modified, and tectonically active slopes are most prone to failure in the Himalayan terrain. Lithology: (1) Katarigali/Manjir, (2) Baliana, (3) Jaunsar, (4) Jutogh, (5) Kulu, (6) Larji, (7) Naraul, (8) Rampur, (9) Shali, (10) Simla, (11) Sirmur, (12) Siwalik, (13) Sunger Nagar, (14) Vaikrita,

4.5 Landslide susceptibility map

A landslide susceptibility map for the Mandi district was produced using the XGB model. The model was categorized into five susceptibility zones: very low, low, moderate, high, and very high (Figure 16), covering 33.4%, 23.9%, 17.5%, 16.6%, and 8.6% of the area, respectively. To evaluate the accuracy of the prediction map, all landslide points in the test data were overlaid on the zoning maps using the Natural Breaks method. The distribution of previous landslides across the various classes of the landslide hazard zoning map is shown in Fig. 17. We found that, with frequency ratios of very high (6.5) and high (1.55), most prior landslides occurred in the very high and high probability classes (>80%).

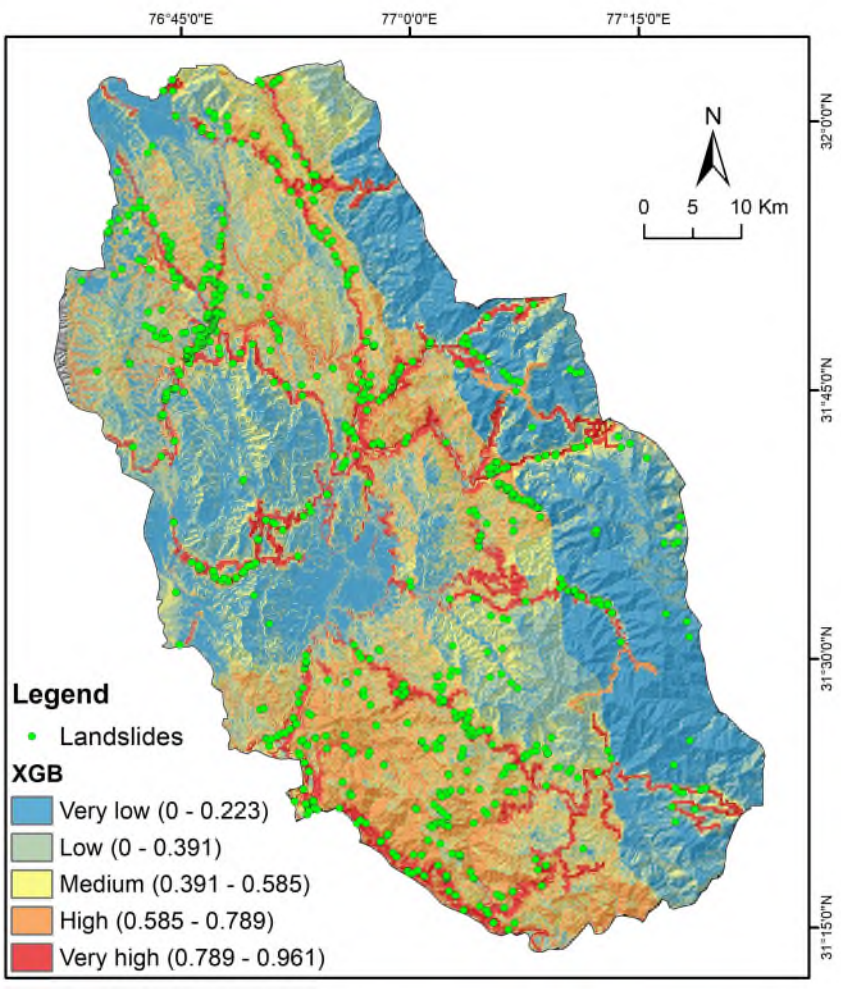


Figure 16 Landslide susceptibility map of Mandi district using the XGB model.

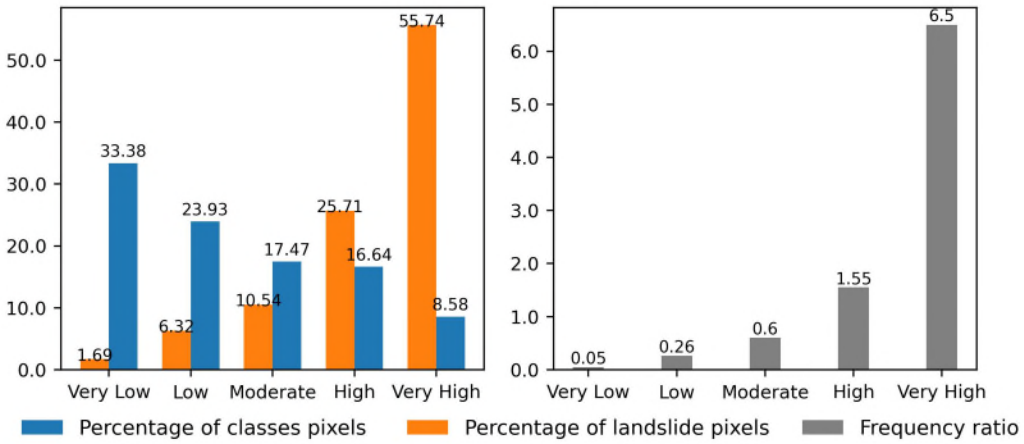


Figure 17: Analysis of landslide density on the susceptibility maps using the XGB model. Frequency ratio (FR) is defined as the ratio between the percentage of landslide occurrences in each class and the percentage of the area occupied by that class.

5. Discussion

5.1 InSAR application in landslide studies

The integration of InSAR and machine learning stems from their complementary strengths. InSAR offers real-time deformation data that identifies active slope processes. At the same time, ML models analyze these movements in relation to predisposing factors. This integration enhances inventory coverage and boosts the model's capacity to predict where and why landslides might happen, effectively bridging the gap between process-based and data-driven methods. In the Mandi district, a landscape shaped by steep mountains, heavy monsoon rains, and shifting tectonic forces, spotting these subtle movements helps us understand not just where landslides have happened, but where they might happen next. Our findings align with and extend previous research demonstrating the utility of InSAR for landslide detection and monitoring, but not for landslide susceptibility mapping [28], [32], [35]. The InSAR-derived deformation products complemented the landslide inventory by identifying actively deforming slopes that are not always detectable through conventional geomorphological mapping, echoing the findings of [28], [29], [32], [35] who noted InSAR's superiority in capturing pre-failure creep in mountainous regions. This highlights the key advantage of InSAR: it captures ongoing ground movement, which shows the land slowly shifting or creeping in real time and improves how we can represent dynamic slope instability processes, meaning the ever-changing factors like water pressure, weathering, and human activity that make slopes gradually weaken and eventually fail. This turns landslide assessment from a static snapshot into a living, evolving picture of risk [31].

Time-series InSAR techniques such as SBAS and PSInSAR have proven effective for detecting slow-to-moderate deformation in both urban and non-urban regions [31], [34]. However, several limitations emerged during our study. Dense vegetation and steep terrain caused localized decorrelation, reducing deformation detection in about 15–20% of the area, mainly in lower-elevation forested zones and deeply incised valleys. This was especially problematic for areas

prone to rapid mass movements, such as debris flows and shallow slides. The decorrelation in these zones highlights a key limitation of C-band SAR in heavily vegetated, dynamic landscapes. Nonetheless, the method maintained high coherence (>0.4) across roughly 70-80% of the district, allowing reliable deformation mapping in bedrock slopes, urban settings, and sparsely vegetated high-altitude terrains.

While InSAR cannot fully capture rapid or complex landslides on its own, it becomes remarkably powerful when combined with field survey, historical records, and machine learning models. InSAR excels at detecting subtle active slopes that show measurable deformation but which may not yet have failed. This means InSAR can spot moving slopes before a full collapse occurs, providing early clues about where future landslides might occur. In our study, we used this InSAR-detected deformation data as training input for machine learning models, which helped predict not only where landslides have occurred before, but also where they are likely to occur next. In short, InSAR doesn't just document past events, it helps forecast future risk, making it a valuable partner in landslide hazard assessment across the Himalayas.

5.2 The importance of landslide conditioning factors

Landslide susceptibility in the Mandi district, Himachal Pradesh, India, is primarily governed by a combination of geological, geomorphological, and anthropogenic factors. Among these, slope, distance to roads, rainfall, faults, and thrusts have emerged as the most significant contributors to slope instability. The findings of this study align with previous research conducted in the Himalayan region [11], [31], further reinforcing the role of these factors in landslide occurrence.

The validation results indicated that the XGB model consistently outperformed the RF and SVM models. Similar findings have been widely reported in previous studies, highlighting XGB's strong predictive performance, its effectiveness in handling missing values, and its robustness to noisy data and outliers. For example, XGB was applied with 10 geospatial conditioning factors to map flood and landslide susceptibility in the River basin, Italy, and used SHAP explainability to interpret influential predictors (elevation, drainage density, lithology) [77]. Also, [78] used this to compare RF, AdaBoost, GBDT, and XGB for landslide susceptibility. XGB achieved the best overall performance (AUC > 0.8, sensitivity ~92.9%). XGB achieved high accuracy (92% landslide classification).

Landslide susceptibility in the Mandi district is primarily controlled by three key factors: slope, distance to roads, and rainfall. Our SHAP and MDA analyses confirm that these are the most influential predictors across all machine learning models. Slopes steeper than 25° had a landslide frequency ratio of 4.3, indicating they were over 4 times more likely to fail. This aligns with regional studies [44], which report similar thresholds in the Himalayan terrain. The distance to roads exhibits a strong negative correlation, with ALE values dropping sharply from about +15 to −10 as the distance increases. This confirms that areas closer to roads are more prone to landslides due to slope cutting, excavation, or drainage modifications associated with infrastructure development [79], [80]. Similarly, the distance to faults decreases with increasing distance, indicating that fault-proximate zones are more vulnerable due to fractured rocks and weakened tectonic conditions [48]. Elevation shows a moderate negative trend, with ALE decreasing from around +8 to −8 as elevation increases, implying that landslides are more frequent at lower elevations where human activity, weathering, and geomorphic factors promote failure. NDVI reveals a steady negative relationship: ALE declines as vegetation density increases, underscoring vegetation's stabilizing effect through root reinforcement and erosion prevention. InSAR data

strengthen these observations: 88% of deformation detected by InSAR occurred in zones where all three main risk factors were unfavorable. Using SHAP values advances beyond traditional frequency-based methods by illustrating not just which factors are important, but also their magnitude and how they interact to trigger landslides (Figures 5, 6, 13).

Overall, the comparison of findings from this study with previous research [11], [79], [80] in the Himalayan region and similar mountainous terrains provides strong confirmation of the significance of slope, distance to roads, and distance to faults, as well as factors like elevation, road proximity, faults, and thrusts as important for landslide triggering. Future research should integrate real-time monitoring systems, high-resolution landslide inventories, and climate change projections to improve landslide susceptibility assessments and enhance disaster preparedness in the region.

5.3 Limitations of this study and future work

Machine learning models, despite their advantages, also have inherent constraints. Each model operates based on certain assumptions and may be susceptible to overfitting, especially in complex terrains with highly variable environmental conditions. Although multiple models were tested, no single algorithm can fully account for all uncertainties in landslide susceptibility prediction.

Furthermore, this study does not incorporate real-time monitoring data, which could enhance the reliability of predictions. The analysis primarily relies on historical records, and future studies should integrate near-real-time satellite observations and ground-based sensor networks to improve landslide forecasting capabilities. Another limitation is the lack of consideration for climate change impacts. Future climatic shifts, such as increased precipitation and extreme weather events, could significantly alter landslide susceptibility patterns. Incorporating climate projections into susceptibility assessments could enhance long-term disaster preparedness.

Despite the valuable insights this study provides, several limitations must be acknowledged. One major constraint is the quality and availability of input data. The accuracy of the landslide susceptibility model heavily depends on high-resolution datasets, including landslide inventories, geological maps, and remote sensing imagery. In some cases, the limited availability of landslide occurrence records may affect the model's predictive performance. However, all the data for the study, other than InSAR data, was taken from the Bhukosh Indian Government open-source portal.

6. Conclusion

This study developed a high-resolution landslide susceptibility map for the Mandi district, Himachal Pradesh, by coupling multi-temporal InSAR deformation analysis (PSI via StaMPS and SBAS via MintPy, 2023–2024) with twelve uncorrelated topographic, hydrological, geological, climatic, and anthropogenic conditioning factors. Among the four machine learning algorithms compared, Extreme Gradient Boosting (XGB) consistently outperformed Random Forest, Logistic Regression, and Multilayer Perceptron under nested spatial block cross-validation, with an optimal block size of 3,000 m. SHAP, mean decrease accuracy, and accumulated local effects analyses identified slope, distance to faults, distance to roads, and rainfall as the dominant controls on landslide occurrence, consistent with the region's steep terrain, dense road network, and active thrust systems. The final five-class map showed that high- and very-high-susceptibility zones, together covering 25.2% of the district, contained the large majority of mapped landslides, with frequency ratios of 1.55 and 6.5, respectively, confirming the model's spatial reliability.

Refining the landslide inventory with InSAR-derived deformation, rather than using it as a direct model input, proved highly effective: 91% of historical landslides coincided with InSAR-detected deformation zones, and the analysis identified 36 previously unmapped, actively deforming slopes, expanding the inventory by 18%. This enhanced inventory improved model AUC by 12–15% relative to a conventional, static inventory, demonstrating that pairing deformation monitoring with conditioning-factor-based machine learning meaningfully strengthens both the completeness and predictive power of susceptibility models.

These gains are nonetheless bounded by C-band signal decorrelation in densely vegetated and steep terrain, which limited reliable deformation detection across roughly 15–20% of the district, together with the largely static nature of the conditioning factors and the absence of real-time monitoring or climate-change projections in the current framework. Future work should incorporate near-real-time InSAR time series, ground-based sensor networks, and downscaled climate projections to further improve predictive accuracy and support proactive disaster preparedness.

To our knowledge, this is the first study to integrate InSAR-derived ground deformation into a machine-learning-based landslide susceptibility framework for Himachal Pradesh. By combining dynamic deformation signals with established geomorphological, hydrological, and anthropogenic conditioning factors, this approach provides a more current and spatially reliable assessment of landslide-prone terrain, supporting hazard mitigation and land-use planning along Mandi district's most vulnerable transportation corridors.

Acknowledgment

The authors acknowledge the Geological Survey of India (GSI) for providing landslide inventory data via the Bhukosh platform and the University of Silesia for institutional support. We acknowledge jUŚt transition for funding the field trip in the study area.

During the preparation of this work, the author(s) used the ChatGPT AI tool for grammar edits. After using this tool/service, the author(s) reviewed and edited the content as needed and took full responsibility for the content of the published article.

Funding

None

Declarations

Conflict of Interest / Competing Interests

The authors declare that they have no known competing financial interests or personal relationships that could have appeared to influence the work reported in this paper.

References

[1] J. Zhou, S. Tan, J. Li, J. Xu, C. Wang, and H. Ye, "Landslide Susceptibility Assessment Using the Analytic Hierarchy Process (AHP): A Case Study of a Construction Site for Photovoltaic Power Generation in Yunxian County, Southwest China," *Sustainability*, vol. 15, no. 6, p. 5281, Mar. 2023, doi: 10.3390/su15065281.

[2] M. Jakob, "Landslides in a changing climate." Accessed: Nov. 16, 2025. [Online]. Available: https://www.sciencedirect.com/science/chapter/edited-volume/abs/pii/B9780128184646000032?via%3Dihub

[3] G. Konapala, A. K. Mishra, Y. Wada, and M. E. Mann, "Climate change will affect global water availability through compounding changes in seasonal precipitation and evaporation," *Nat. Commun.*, vol. 11, no. 1, p. 3044, Jun. 2020, doi: 10.1038/s41467-020-16757-w.

[4] F. Fusco *et al.*, "Hydrological regimes in different slope environments and implications on rainfall thresholds triggering shallow landslides," *Nat. Hazards*, vol. 114, no. 1, pp. 907–939, Jun. 2022, doi: 10.1007/s11069-022-05417-5.

[5] O. Marc, A. Stumpf, J.-P. Malet, M. Gosset, T. Uchida, and S.-H. Chiang, "Initial insights from a global database of rainfall-induced landslide inventories: the weak influence of slope and strong influence of total storm rainfall," *Earth Surf. Dyn.*, vol. 6, pp. 903–922, Oct. 2018, doi: 10.5194/esurf-6-903-2018.

[6] D. Rotheram-Clarke, D. Huntley, P. LeSueur, R. Cocking, and J. Joseph, "Direct Comparison of Insar, UAV & RTK Deformation Methods at North Slide, Thompson River Valley, British Columbia, Canada," in *IGARSS 2023 - 2023 IEEE International Geoscience and Remote Sensing Symposium*, Jul. 2023, pp. 2858–2861. doi: 10.1109/IGARSS52108.2023.10283213.

[7] E. Sana, A. Kumar, E. Robson, R. Prasanna, U. Kala, and D. G. Toll, "Preliminary assessment of a series of landslides and related damage by heavy rainfall in Himachal Pradesh, India, during July 2023," *Landslides*, vol. 21, no. 4, pp. 919–931, Apr. 2024, doi: 10.1007/s10346-023-02209-1.

[8] K. Chand and D. D. Sharma, "Spatial Pattern of Landslide Vulnerability at Block Level in District Mandi of Himachal Pradesh: A GIS-Based Approach," vol. 1, 2017.

[9] P. Reichenbach, M. Rossi, B. D. Malamud, M. Mihir, and F. Guzzetti, "A review of statistically-based landslide susceptibility models," *Earth-Sci. Rev.*, vol. 180, pp. 60–91, May 2018, doi: 10.1016/j.earscirev.2018.03.001.

[10] M. Ado *et al.*, "Landslide Susceptibility Mapping Using Machine Learning: A Literature Survey," *Remote Sens.*, vol. 14, no. 13, p. 3029, Jun. 2022, doi: 10.3390/rs14133029.

[11] A. Singh, N. Dhiman, N. K.C., and D. Shukla, "'Ensembled transfer learning approach for error reduction in landslide susceptibility mapping of the data scarce region,'" *Sci. Rep.*, vol. 14, Nov. 2024, doi: 10.1038/s41598-024-76541-4.

[12] H. Bhardwaj and M. Thakur, "Slope stability analysis of the Mandi Landslide, Mandi, Himachal Pradesh, India," *Discov. Geosci.*, vol. 3, no. 1, p. 146, Oct. 2025, doi: 10.1007/s44288-025-00258-8.

[13] A. R. Manocha, N. Kumar, and A. Kumar, "Spline-Based Volume Estimation of landslides Using Different DEMs: Case Studies of the Kotropi and Prashar Lake Landslides, Northwestern Himalaya," 2025.

[14] S. Kahlon, "Landslides in Himalayan Mountains: A Study of Himachal Pradesh, India," *Int. J. IT Eng. Appl. Sci. Res.*, vol. 3, pp. 28–34, Jan. 2014.

[15] S. Verma and V. S. Khanduri, “GIS-Based Study To Develop Landslide Susceptibility Zonation Map Of District Mandi, Himachal Pradesh,” Jun. 24, 2021, *In Review*. doi: 10.21203/rs.3.rs-588435/v1.
[16] A. S. Prasad, B. W. Pandey, W. Leimgruber, and R. M. Kunwar, “Mountain hazard susceptibility and livelihood security in the upper catchment area of the river Beas, Kullu Valley, Himachal Pradesh, India,” *Geoenvironmental Disasters*, vol. 3, no. 1, pp. 1–17, Feb. 2016, doi: 10.1186/s40677-016-0037-x.
[17] H. bureau, “Mandi records 1939% excess rainfall on July 1; Himachal logs one of the wettest days of the season.” Accessed: Jan. 16, 2026. [Online]. Available: https://himachalscape.com/himachal-records-56-percent-more-rain-than-normal-from-june-1-to-july-1-mandi-150-percent-excess/
[18] N. Mali, D. Shukla, and U. Kala, “Identifying Geotechnical Characteristics for Landslide Hazard Indication: A Case Study in Mandi, Himachal Pradesh, India,” *Arab. J. Geosci.*, vol. 15, Jan. 2022, doi: 10.1007/s12517-022-09475-8.
[19] N. Singh, S. K. Gupta, and D. P. Shukla, “ANALYSIS OF LANDSLIDE REACTIVATION USING SATELLITE DATA: A CASE STUDY OF KOTRUPI LANDSLIDE, MANDI, HIMACHAL PRADESH, INDIA,” *Int. Arch. Photogramm. Remote Sens. Spat. Inf. Sci.*, vol. XLII-3-W11, pp. 137–142, Feb. 2020, doi: 10.5194/isprs-archives-XLII-3-W11-137-2020.
[20] O. N. Bhargava and S. V. Srikantia, “Geology and age of metamorphism of the Jutogh and Vaikrita Thrust Sheets, Himachal Himalaya,” *Himal. Geol.*, vol. 35, pp. 1–15, Jan. 2014.
[21] I. Mukherjee, C. Montomoli, R. Carosi, R. Law, S. Singh, and S. Man, “The Higher Himalayan Crystallines, Alaknanda – Dhauli Gan-ga Valleys, Garhwal Himalaya, India,” *J. Virtual Explor.*, vol. 47, Mar. 2014.
[22] R. Patel, V. Adlakha, P. Singh, Y. Kumar K, and N. Lal, “Geology, Structural and Exhumation History of the Higher Himalayan Crystallines in Kumaon Himalaya, India,” *J. Geol. Soc. India*, vol. 77, pp. 47–72, Mar. 2011, doi: 10.1007/s12594-011-0008-5.
[23] O. N. Bhargava and U. K. Bassi, “The Crystalline Thrust Sheets in the Himachal Himalaya and the Age of Amphibolite Facies Metamorphism,” *J. Geol. Soc. India*, vol. 43, pp. 343–352, Apr. 1994, doi: 10.17491/jgsi/1994/430403.
[24] C. S. Dubey, K. Venkatachalam, M. Ratnam, and P. Shekhar, “Causes of seepage water in drainage and grouting galleries of the Pandoh Dam, Central Himalaya,” 2004, Accessed: Jan. 05, 2026. [Online]. Available: https://www.academia.edu/9913280/Causes_of_seepage_water_in_drainage_and_grouting_galleries_of_the_Pandoh_Dam_Central_Himalaya
[25] A. Kundu, N. Pant, and S. Joshi, “Palaeozoic granites and their younger components - A study of Mandi and Rakcham granites from the Himachal Himalaya,” *Himal. J. Sci.*, vol. 5, Sep. 2008, doi: 10.3126/hjs.v5i7.1278.
[26] H. Shankar *et al.*, “Multi-temporal InSAR and Sentinel-1 for assessing land surface movement of Joshimath town, India,” *Geomat. Nat. Hazards Risk*, vol. 14, no. 1, p. 2253972, Dec. 2023, doi: 10.1080/19475705.2023.2253972.
[27] A. Hooper, P. Segall, and H. Zebker, “Persistent scatterer interferometric synthetic aperture radar for crustal deformation analysis, with application to Volcán Alcedo, Galápagos,” *J. Geophys. Res. Solid Earth*, vol. 112, no. B7, 2007, doi: 10.1029/2006JB004763.
[28] R. Dwivedi, P. Varshney, A. Tiwari, A. K. Singh, and O. Dikshit, “ISPRS-Archives - Assessment of slope stability using PS-InSAR technique,” 2014, Accessed: Jan. 05, 2026.

[Online]. Available: https://isprs-archives.copernicus.org/articles/XL-8/35/2014/?utm_source=chatgpt.com
[29] R. Dwivedi, A. B. Narayan, A. Tiwari, O. Dikshit, and A. K. Singh, "ISPRS-Archives - MULTI-TEMPORAL SAR INTERFEROMETRY FOR LANDSLIDE MONITORING," 2016, Accessed: Jan. 05, 2026. [Online]. Available: https://isprs-archives.copernicus.org/articles/XLI-B8/55/2016/
[30] S. K. P V, D. Kim, and Y. Kim, "Time-series InSAR Analysis and Post-processing Using ISCE-StaMPS Package for Measuring Bridge Displacements," *Korean J. Remote Sens.*, vol. 36, pp. 527–534, Sep. 2020, doi: 10.7780/kjrs.2020.36.4.3.
[31] J. Yao, X. Yao, and X. Liu, "Landslide Detection and Mapping Based on SBAS-InSAR and PS-InSAR: A Case Study in Gongjue County, Tibet, China," *Remote Sens.*, vol. 14, no. 19, p. 4728, Sep. 2022, doi: 10.3390/rs14194728.
[32] Z. Yunjun, H. Fattahi, and F. Amelung, *Small baseline InSAR time series analysis: Unwrapping error correction and noise reduction*. 2019. doi: 10.31223/osf.io/9sz6m.
[33] S. Sharifi, R. Macciotta, and M. Hendry, *InSAR landslide monitoring using SNAP- MintPy: case studies of Assiniboine and Thompson River Valleys*. 2024.
[34] Y. Yi, X. Xu, G. Xu, and H. Gao, "Rapid Mapping of Slow-Moving Landslides Using an Automated SAR Processing Platform (HyP3) and Stacking-InSAR Method," *Remote Sens.*, vol. 15, no. 6, p. 1611, Mar. 2023, doi: 10.3390/rs15061611.
[35] M. Manunta *et al.*, "The Parallel SBAS Approach for Sentinel-1 Interferometric Wide Swath Deformation Time-Series Generation: Algorithm Description and Products Quality Assessment," *IEEE Trans. Geosci. Remote Sens.*, vol. 57, no. 9, pp. 6259–6281, Sep. 2019, doi: 10.1109/TGRS.2019.2904912.
[36] Bhukosh, "Geological Survey of India, Government of India, Kolkata, India- Bhukosh DataSet." 2025.
[37] F. C. Dai and C. F. Lee, "Terrain-based Mapping of Landslide Susceptibility Using a Geographical Information System: A Case Study," *Can. Geotech. J.*, vol. 38, no. 5, 2001.
[38] M. Ercanoglu, C. Gokceoglu, and Th. W. J. Asch, "Landslide Susceptibility Zoning North of Yenice (NW Turkey) by Multivariate Statistical Techniques," *Nat. Hazards*, vol. 32, pp. 1–23, May 2004, doi: 10.1023/B:NHAZ.0000026786.85589.4a.
[39] U. Kamp, B. J. Growley, G. A. Khattak, and L. A. Owen, "GIS-based landslide susceptibility mapping for the 2005 Kashmir earthquake region," *Geomorphology*, vol. 101, no. 4, pp. 631–642, Nov. 2008, doi: 10.1016/j.geomorph.2008.03.003.
[40] N. Saadatkhah, A. Kassim, and L. Lee, "Qualitative and quantitative landslide susceptibility assessments in Hulu Kelang area, Malaysia," *Electron. J. Geotech. Eng.*, vol. 19, pp. 545–563, Jan. 2014.
[41] H. Yu *et al.*, "Integrated InSAR and Machine Learning Reveal Soil Type as Primary Control on Rainfall-Triggered Landslide Susceptibility in Meizhou, China," *Land Degrad. Dev.*, p. n/a-n/a, Dec. 2025, doi: 10.1002/ldr.70360.
[42] J. G. Masek *et al.*, "Landsat 9: Empowering open science and applications through continuity," *Remote Sens. Environ.*, vol. 248, p. 111968, Oct. 2020, doi: 10.1016/j.rse.2020.111968.
[43] A. Yalcin, S. Reis, A. C. Aydinoglu, and T. Yomralioglu, "A GIS-based comparative study of frequency ratio, analytical hierarchy process, bivariate statistics and logistics regression methods for landslide susceptibility mapping in Trabzon, NE Turkey," *CATENA*, vol. 85, no. 3, pp. 274–287, Jun. 2011, doi: 10.1016/j.catena.2011.01.014.

[44] M. Basharat, J. Rohn, M. Baig, M. Rustam Khan, and M. Schleier, “Large scale Mass movements triggered by the Kashmir Earthquake 2005, Pakistan,” *J. Mt. Sci.*, vol. 11, pp. 19–30, Feb. 2014, doi: 10.1007/s11629-012-2629-6.
[45] H. A. Nefeslioglu, C. Gokceoglu, and H. Sonmez, “An assessment on the use of logistic regression and artificial neural networks with different sampling strategies for the preparation of landslide susceptibility maps,” *Eng. Geol.*, vol. 97, no. 3, pp. 171–191, Apr. 2008, doi: 10.1016/j.enggeo.2008.01.004.
[46] M. Maggioni and U. Gruber, “The influence of topographic parameters on avalanche release dimension and frequency,” *Cold Reg. Sci. Technol.*, vol. 37, no. 3, pp. 407–419, Nov. 2003, doi: 10.1016/S0165-232X(03)00080-6.
[47] H. Vijith, K. N. Krishnakumar, G. S. Pradeep, M. V. Ninu Krishnan, and G. Madhu, “Shallow landslide initiation susceptibility mapping by GIS-based weights-of-evidence analysis of multi-class spatial data-sets: a case study from the natural sloping terrain of Western Ghats, India,” *Georisk Assess. Manag. Risk Eng. Syst. Geohazards*, vol. 8, no. 1, pp. 48–62, Jan. 2014, doi: 10.1080/17499518.2013.843437.
[48] C. Guo, D. R. Montgomery, Y. Zhang, K. Wang, and Z. Yang, “Quantitative assessment of landslide susceptibility along the Xianshuihe fault zone, Tibetan Plateau, China,” *Geomorphology*, vol. 248, pp. 93–110, Nov. 2015, doi: 10.1016/j.geomorph.2015.07.012.
[49] B. Lehner and G. Grill, “Global river hydrography and network routing: baseline data and new approaches to study the world’s large river systems,” *Hydrol. Process.*, vol. 27, no. 15, pp. 2171–2186, 2013, doi: 10.1002/hyp.9740.
[50] C. Funk *et al.*, “The climate hazards infrared precipitation with stations—a new environmental record for monitoring extremes,” *Sci. Data*, vol. 2, no. 1, p. 150066, Dec. 2015, doi: 10.1038/sdata.2015.66.
[51] H. Hamedi, A. Alesheikh, M. Panahi, and S. Lee, “Landslide susceptibility mapping using deep learning models in Ardabil province, Iran,” *Stoch. Environ. Res. Risk Assess.*, vol. 36, Jun. 2022, doi: 10.1007/s00477-022-02263-6.
[52] H. Ha, B. Duy Quynh, D. Tran, H. Bui Xuan, and C. Luu, “Improving the forecast performance of landslide susceptibility mapping by using ensemble gradient boosting algorithms,” *Environ. Dev. Sustain.*, vol. 27, pp. 18409–18443, Mar. 2024, doi: 10.1007/s10668-024-04694-3.
[53] I. Behera, N. Jain, T. R. Martha, and M. Bose, “Optimising sampling strategies for AI-based landslide susceptibility mapping: a case study of Idukki, Kerala,” *Nat. Hazards*, vol. 122, no. 1, p. 18, Dec. 2025, doi: 10.1007/s11069-025-07842-8.
[54] Z. Guo, B. Tian, Y. Zhu, J. He, and T. Zhang, “How do the landslide and non-landslide sampling strategies impact landslide susceptibility assessment? — A catchment-scale case study from China,” *J. Rock Mech. Geotech. Eng.*, vol. 16, no. 3, pp. 877–894, Mar. 2024, doi: 10.1016/j.jrmge.2023.07.026.
[55] O. Korup and A. Stolle, “Landslide prediction from machine learning,” *Geol. Today*, vol. 30, no. 1, pp. 26–33, 2014, doi: 10.1111/gto.12034.
[56] P. Probst, A.-L. Boulesteix, and B. Bischl, “Tunability: Importance of Hyperparameters of Machine Learning Algorithms,” 2019.
[57] C. Molnar, “Interpretable Machine Learning.” Accessed: Jan. 05, 2026. [Online]. Available: https://christophm.github.io/interpretable-ml-book/
[58] T. Chen and C. Guestrin, “XGBoost: A Scalable Tree Boosting System,” in *Proceedings of the 22nd ACM SIGKDD International Conference on Knowledge Discovery and Data*

Mining, in KDD '16. New York, NY, USA: Association for Computing Machinery, Aug. 2016, pp. 785–794. doi: 10.1145/2939672.2939785.
[59] J. Friedman, "Greedy Function Approximation: A Gradient Boosting Machine," *Ann. Stat.*, vol. 29, Nov. 2000, doi: 10.1214/aos/1013203451.
[60] L. Breiman, "Random Forests," *Mach. Learn.*, vol. 45, no. 1, pp. 5–32, Oct. 2001, doi: 10.1023/A:1010933404324.
[61] T. Hengl, M. Nussbaum, M. N. Wright, G. B. M. Heuvelink, and B. Gräler, "Random forest as a generic framework for predictive modeling of spatial and spatio-temporal variables," 2018, Accessed: Jan. 05, 2026. [Online]. Available: https://peerj.com/articles/5518
[62] G. Biau and E. Scornet, "A random forest guided tour," *TEST*, vol. 25, no. 2, pp. 197–227, Apr. 2016, doi: 10.1007/s11749-016-0481-7.
[63] V. N. Vapnik, "The Nature of Statistical Learning Theory | Springer Nature Link." Accessed: Jan. 13, 2026. [Online]. Available: https://link.springer.com/book/10.1007/978-1-4757-3264-1
[64] X. Yao, L. G. Tham, and F. C. Dai, "Landslide susceptibility mapping based on Support Vector Machine: A case study on natural slopes of Hong Kong, China," *Geomorphology*, vol. 101, no. 4, pp. 572–582, Nov. 2008, doi: 10.1016/j.geomorph.2008.02.011.
[65] N. Regmi, R. Giardino, E. Mcdonald, and J. Vitek, "A comparison of logistic regression-based models of susceptibility to landslides in western Colorado, USA," *Landslides*, vol. 11, Jan. 2010, doi: 10.1007/s10346-012-0380-2.
[66] D. Li, F. Huang, L. Yan, Z. Cao, J. Chen, and Z. Ye, "Landslide Susceptibility Prediction Using Particle-Swarm-Optimized Multilayer Perceptron: Comparisons with Multilayer-Perceptron-Only, BP Neural Network, and Information Value Models," *Appl. Sci.*, vol. 9, no. 18, p. 3664, Sep. 2019, doi: 10.3390/app9183664.
[67] T. V. Phong *et al.*, "Landslide susceptibility modeling using different artificial intelligence methods: a case study at Muong Lay district, Vietnam," *Geocarto Int.*, vol. 36, no. 15, pp. 1685–1708, Sep. 2021, doi: 10.1080/10106049.2019.1665715.
[68] E. Alpaydin, *Machine Learning, revised and updated edition*. MIT Press, 2021.
[69] S. M. Lundberg and S.-I. Lee, "A Unified Approach to Interpreting Model Predictions," in *Advances in Neural Information Processing Systems*, Curran Associates, Inc., 2017. Accessed: Dec. 23, 2025. [Online]. Available: https://proceedings.neurips.cc/paper_files/paper/2017/hash/8a20a8621978632d76c43dfd28b67767-Abstract.html
[70] H. Han, X. Guo, and H. Yu, "Variable selection using Mean Decrease Accuracy and Mean Decrease Gini based on Random Forest," in *2016 7th IEEE International Conference on Software Engineering and Service Science (ICSESS)*, Aug. 2016, pp. 219–224. doi: 10.1109/ICSESS.2016.7883053.
[71] R. Das, P. V. Tien, K. W. Wegmann, and M. Chakraborty, "Machine learning-based assessment of regional-scale variation of landslide susceptibility in central Vietnam," 2024, doi: 10.1371/journal.pone.0308494.
[72] D. W. Apley and J. Zhu, "Visualizing the Effects of Predictor Variables in Black Box Supervised Learning Models," *J. R. Stat. Soc. Ser. B Stat. Methodol.*, vol. 82, no. 4, pp. 1059–1086, Sep. 2020, doi: 10.1111/rssb.12377.
[73] S. Bai, J. Wang, L. G.N, Z. Gen, S.-S. Hou, and S.-N. Xu, "GIS-based and logistic regression for landslide susceptibility mapping of Zhongxian segment in the Three Gorge

area,China," *Geomorphology*, vol. 115, pp. 23–31, Feb. 2010, doi: 10.1016/j.geomorph.2009.09.025.
[74] S. E. Ramani, K. Pitchaimani, and V. R. Gnanamanickam, "GIS based landslide susceptibility mapping of Tevankarai Ar sub-watershed, Kodaikkanal, India using binary logistic regression analysis," *J. Mt. Sci.*, vol. 8, no. 4, pp. 505–517, Jul. 2011, doi: 10.1007/s11629-011-2157-9.
[75] E. R. Sujatha and V. Sridhar, "Landslide Susceptibility Analysis: A Logistic Regression Model Case Study in Coonoor, India," *Hydrology*, vol. 8, no. 1, p. 41, Mar. 2021, doi: 10.3390/hydrology8010041.
[76] B. Youssef *et al.*, "The contribution of the frequency ratio model and the prediction rate for the analysis of landslide risk in the Tizi N'tichka area on the national road (RN9) linking Marrakech and Ouarzazate," *CATENA*, vol. 232, p. 107464, Nov. 2023, doi: 10.1016/j.catena.2023.107464.
[77] M. Rondinone *et al.*, "Assessing Flood and Landslide Susceptibility Using XGBoost: Case Study of the Basento River in Southern Italy," *Appl. Sci.*, vol. 15, no. 10, p. 5290, May 2025, doi: 10.3390/app15105290.
[78] A. Wei, K. Yu, F. Dai, F. Gu, W. Zhang, and Y. Liu, "Application of Tree-Based Ensemble Models to Landslide Susceptibility Mapping: A Comparative Study," *Sustainability*, vol. 14, no. 10, p. 6330, May 2022, doi: 10.3390/su14106330.
[79] P. T. Jallayu, A. Sharma, and K. Singh, "Vulnerability of highways to landslide using landslide susceptibility zonation in GIS: Mandi district, India," *Innov. Infrastruct. Solut.*, vol. 9, no. 9, p. 354, Aug. 2024, doi: 10.1007/s41062-024-01653-9.
[80] S. Saha, A. Saha, T. K. Hembram, B. Pradhan, and A. M. Alamri, "Evaluating the Performance of Individual and Novel Ensemble of Machine Learning and Statistical Models for Landslide Susceptibility Assessment at Rudraprayag District of Garhwal Himalaya," *Appl. Sci.*, vol. 10, no. 11, p. 3772, May 2020, doi: 10.3390/app10113772.
[81] Sun Kai, Hu Y, Lakhanpal G, Zhou R (2023) Spatial Cross-Validation for GeoAI. 1–15. https://doi.org/10.1201/9781003308423-10